Draft for ApJ

An Effective Temperature Scale for Late M and L Dwarfs, from Resonance Absorption Lines of Cs I and Rb I

Gibor Basri[1], Subhanjoy Mohanty[1], France Allard[2], Peter H. Hauschildt[3], Xavier Delfosse[4,5], Eduardo L. Martín[1], Thierry Forveille[4], Bertrand Goldman[6]

ABSTRACT

We present Keck HIRES spectra of 6 late-M dwarfs and 11 L dwarfs. Our goal is to assign effective temperatures to the objects using detailed atmospheric models and fine analysis of the alkali resonance absorption lines of Cs I and Rb I . These yield mutually consistent results (± 150 K) when we use "cleared-dust" models, which account for the removal of refractory species from the molecular states but do not include dust opacities. We find a tendency for the Rb I line to imply a slightly higher temperature, which we ascribe to an incomplete treatment of the overlying molecular opacities. This work, in combination with results from the infrared, hints that dust in these atmospheres has settled out of the high atmosphere but is present in the deep photosphere. We also derive radial and rotational velocities for all the objects, finding that the previously discovered trend of rapid rotation for very low mass objects is quite pervasive. To improve on our analysis, there is a clear need for better molecular line lists and a more detailed understanding of dust formation and dynamics.

Subject headings: stars:evolution — stars:fundamental parameters — stars:low-mass, brown dwarfs

---

[1]Astronomy Department, University of California, Berkeley, CA 94720. basri@soleil.berkeley.edu; subu@astron.berkeley.edu; ege@gps.caltech.edu

[2]C.R.A.L (UML 5574) Ecole Normale Superieure, 69364 Lyon Cedex 7, France. fallard@ens-lyon.fr

[3]Dept. of Physics & Astronomy & Center for Simulational Physics, University of Georgia, Athens, GA 30602-2451. yeti@hal.physast.uga.edu

[4]Observatoire de Grenoble, 414 rue de la Piscine, Domaine Universitaire de St. Martin d'Hères, F-38041 Grenoble, France. Thierry.Forveille@obs.ujf-grenoble.fr

[5]Instituto de Astrofísica de Canarias, E-38200 La Laguna, Tenerife, Canary Islands, Spain. delfosse@ll.iac.es

[6]CEA, DSM, DAPNIA, Centre d'Études de Saclay, 91191 Gif-sur-Yvette Cedex, France. bgoldman@cea.fr

1. Introduction

M dwarfs are among the faintest and coolest stellar objects. Their optical spectra are dominated by molecular band absorption. The major opacity sources in the optical regions are TiO and VO bands, which produce a pseudo-continuum with the atomic lines superposed. Recent surveys (e.g. DENIS, 2MASS) have turned up even cooler objects, including brown dwarfs (Delfosse et al. 1999; Kirkpatrick et al. 1999a). The optical spectra of these objects are still characterized by molecular band absorption; however, the TiO and VO bands, which constitute the defining characteristic of the M spectral class, become very weak or are absent, while the metal hydrides begin to dominate. This is presumably because of the depletion of heavy elements in their cool photospheres through the formation (and perhaps subsequent gravitational settling) of dust grains, especially solid VO and perovskite ($CaTiO_3$) (Sharp & Huebner 1990; Tsuji et al. 1996b; Allard 1998). For this reason, a new spectral class, 'L', has been proposed for these very cool low-mass objects (Martín et al. 1997; Kirkpatrick et al. 1999a; Martín et al. 1999b).

To understand these very cool, low mass stellar and substellar objects, it is necessary to assign to them an effective temperature scale. This has been attempted in recent years by comparing their spectra to synthetic ones generated by atmospheric models. Comparisons have been made on the basis of spectral energy distributions (SEDs) (Tinney et al. 1998; Ruiz et al. 1997) and infrared colors (Leggett et al. 1998). Attempts have also been made to construct a temperature scale using the molecular lines in the observed spectra, since these are sensitive to photospheric temperature. Tinney et al. 1998 do this in the optical by ranking the objects in order of TiO, VO, CrH and FeH equivalent widths; Delfosse et al. 1999 pursue a similar program in the infrared by using H_2O indices. Tokunaga & Kobayashi 1999 do so with a spectral color index based on moderate dispersion spectroscopy in the K band. Kirkpatrick et al. 1999a have performed a detailed analysis of low dispersion optical spectra as a first step towards defining the subclasses of the L spectral type.

It is found that the models fit the observed SEDs and colors fairly well overall, and an effective temperature scale is indeed derivable from the fits. As T_{eff} decreases from early to late spectral types, some molecular bands which comprise most of the low resolution spectral features of these cool objects first increase and then decrease in strength due to dust formation (both through depletion from the gas phase and heating effects). The broadband infrared color indices (eg. J-K or I-K) saturate at very cool temperatures, and eventually also reverse direction (though it seems that I-Z or I-J might be monotonic with temperature). The molecular line lists in the models are not fully satisfactory, which could affect the temperature scale. It is therefore useful to have an alternative and complementary way of estimating effective temperatures.

We present such a method here: fitting synthetic spectra to the profiles of strong atomic alkali lines. Their extremely low ionization potential allows the alkali metals (Li, Na, K, Cs and Rb) to remain neutral only at low temperatures. More importantly, their atomic resonance lines occur in the red and are thus prominent in very cool photospheres, displaying deep cores and broad wings in high-resolution spectra. Finally and most importantly, the alkali metals are relatively undepleted by dust formation, and their resonance lines are apparently formed in photospheric layers located above the region affected most by dust. For these reasons, the resonance features of the alkali metals are excellent temperature indicators in cool photospheres, and grow monotonically in strength with decreasing temperature in the range of interest. We therefore attempt to assign effective temperatures to 17 late-M and L dwarfs by fitting model spectra to their Cs I and Rb I high-resolution line-profiles.

In principle, the Na I and K I lines can be also be used for this purpose. However, we have not considered them in this paper, for the following reasons. The K I line in some of our sample objects is very broad, extending beyond one whole echelle order. To fit models to it, neighboring orders must be patched together, a task fraught with sources of error and thus considered too risky for the fine-analysis we undertake here. We do not have observations of the Na I spectral section for a number of our sample objects due to incomplete coverage of the echelle format by the current CCD in HIRES. Therefore, we consider only the Cs I and Rb I lines in this paper. We hope to pursue an investigation of the Na I and K I lines in the future.

The synthetic spectra we use are generated by the atmospheric models of Allard and Hauschildt (hereafter AH). The models come with 3 treatments: "standard (no-dust)", "dusty" and "cleared-dust" (discussed in §3). The first does not account for dust formation at all, while the second takes dust formation into account by considering both dust grain opacities and photospheric depletion of dust-forming elements (physically, this implies a haze of dust that is mixed throughout the atmosphere). The third ignores dust opacities but accounts for elemental depletion, simulating the state of affairs when dust forms and then gravitationally settles below the photosphere. We will show that the "standard" and "dusty" models only poorly reproduce the optical observations – the alkali lines in the first are too narrow and in the second they are too weak to fit most observations. The "cleared-dust" models, however, fit the data much better.

2. Observations

2.1. Sample

Until 1997, the only L-type object known was GD165B (Becklin & Zuckerman 1988), although it was not identified with that sobriquet. Indeed, a good spectral analysis of it has only recently appeared (Kirkpatrick et al. 1999b). All the L dwarfs studied in this paper, therefore, are recent discoveries. They come primarily from the DENIS all-sky IR southern survey (Delfosse et al. 1999; Martín et al. 1999b). Some are from other sources. Kelu-1 (Ruiz et al. 1997) was announced as the first confirmed field brown dwarf; it was found in a proper motion survey of faint red objects. LP 944-20 is a late M star from the Luyten proper motion survey, which Tinney 1998 discovered contains lithium, making it a brown dwarf. G196-3 is a brown dwarf companion to a nearby young M star found by Rebolo et al. 1998; this is among the lowest mass brown dwarfs currently imaged. LHS 102B is an L dwarf companion to another nearby M star, found by a proper motion study of the EROS project's images (Goldman et al. 1999). Recently, the 2MASS project has greatly added to the inventory of L stars (Kirkpatrick et al. 1999a). Thus, our sample is not selected in any particular way, but is a first look at objects out of the initial discovery list of cool VLM field objects. The list of objects observed is given in Table 1. There are new objects being discovered monthly now by the DENIS, 2MASS, and Sloan surveys; it will soon be possible to study samples chosen in a more statistically meaningful way.

2.2. Data Acquisition and Reduction

Observations were made with the W. M. Keck I 10-m telescope on Mauna Kea using the HIRES echelle spectrometer (Vogt et al. 1994). The observation dates are listed in Table 1. The instrument yielded 15 spectral orders from 640nm to 860nm (with gaps between orders), detected with a Tektronix 2048^2 CCD. The CCD pixels are $24\mu m$ in size and were binned 2×2; the bins are hereafter referred to as individual "pixels". Each pixel covered 0.1A, and use of slit decker "D1" gave a slit width of 1.15 arcsec projected on the sky, corresponding to 2 pixels on the CCD and a spectral resolution of R = 31000. The slit length is 14 arcsec, allowing excellent sky subtraction. The CCD exhibited a dark count of $\sim$2 e-/h and a readout noise of 5 e-/pixel.

The data were reduced in a standard fashion for echelle spectra, using IDL procedures. This includes flat-fielding with a quartz lamp, order definition and extraction and sky subtraction. The stellar slit function is found in the redmost order, and used to perform a weighted extraction in all orders. The wavelength scale is established using a ThAr spectrum taken without moving the grating; the solution is a 2-D polynomial fit good to 0.3 pixels or better everywhere. Cosmic-ray hits and other large noise-spikes were removed using an upward median correction routine, wherein points more than 7σ above the median (calculated in 9-pixel bins) were discarded. All points below the median were retained, to preserve the integrity of sharp absorption lines.

For the purpose of comparing data to models, it is necessary to normalize both to the same continuum value. However, the continuum in the data and the models is characterized by a large number of overlapping molecular lines; moreover, the data is not flux-calibrated, and has a superimposed echelle blaze function. Thus, only a pseudo-continuum is derivable for the data and models. A straight-line fit to the pseudo-continuum was obtained for each observed spectrum, and divided out for normalization. The fit was made after manually discarding strong spectral lines (selected by eye), including the alkali absorption lines. For Cs I , the overall fit was obtained in the range 8500-8540A; for Rb I , in the range 7930-7960A.

2.3. Radial Velocities

Barycentric and stellar radial velocity corrections were derived for each observed spectrum. We thank G. Marcy for the IDL routine which calculates the barycentric correction. The radial velocities were derived by measuring the peak position for cross-correlation functions between each star and a radial velocity standard. We chose Gl 406 (M6) as our standard for the M and early L-dwarfs, and 2MASSW 1439+1929 as our standard for the L-dwarfs later than L1.

Gl406 was chosen as a standard since its velocity has been given by several authors to good accuracy. In particular, Delfosse has found it to be +19 km s^{-1} as part of his precision radial velocity project. Measurement of the Cs I line shift on an absolute wavelength scale for our December 1997 observation of Gl406 yielded a velocity of +19 km s^{-1} , and a velocity of +43 km s^{-1} for the spectrum observed in June 1997 (with an accuracy of about 3km s^{-1}). A previous spectrum taken by Basri in November 1993 gives +18 km s^{-1} , and a new spectrum observed in June 1999 also gives +18 km s^{-1} (using the December 1997 spectrum as calibrator). We examined the discrepant velocity of June 1997, comparing the ThAr spectra and night sky spectra for the 2 nights to confirm that the grating had not moved from where we thought it was. There is a clear shift of the star compared with night sky lines on the same echelle frames for the two epochs. The stellar spectra themselves are otherwise almost identical.

Radial velocities of all the other objects were obtained by cross-correlation with each of the two 1997 Gl 406 spectra, in the spectral interval 8630 - 8753A (containing TiO, VO, CrH and FeH lines). The December 1997 and June 1997 observations of Gl 406 jointly yield consistent radial velocities for the other objects (within ± 5 km s^{-1}) when employed separately. Delfosse, however, has not seen radial velocity variations in his precision observations of Gl 406, including one only a few months away from those reported here. Either Gl 406 is a radial velocity variable, or we happened to observe a near twin quite close by (none is known). Tinney & Reid 1998 obtained an "inexplicable" discrepancy in velocity for GJ 1111 compared to other published results. Such behavior could result if these are highly eccentric single-lined spectroscopic binaries. Clearly these systems bear closer monitoring.

Since the spectrum of the cooler objects in our sample (Kelu-1, DENIS-P J1058-1548, LHS 102B, DENIS-P J1228-1547, DENIS-P J0205-1159, DENIS-P J0255-4700, 2MASSW 1146+2230 and 2MASSW 1632+1904) in the given interval is not very similar to that of Gl 406 (as TiO and VO disappear and CrH and FeH appear with decreasing temperature), cross-correlation for these objects was carried out using 2MASSW 1439+1929 as the standard, and radial velocities were then calculated using the radial velocity of -30 km s^{-1} obtained for 2MASSW 1439+1929 by cross-correlation with the June 1999 Gl 406 spectrum.

3. Model Atmospheres

As photospheric temperatures decrease, atoms combine to form molecules; upon still further cooling, atoms and molecules may coagulate to form dust grains. Dust formation can change the atmospheric spectral characteristics in various ways. For example, grains can warm the photosphere by backwarming, making the spectral distribution redder while weakening molecular lines (e.g., of H_2O and TiO) (Jones & Tsuji 1997; Tsuji et al. 1996a). Dust formation decreases the photospheric gas phase abundance of the atoms that form dust (e.g. Ti, Ca, Al, Mg, Si, Fe). Furthermore, with decreasing temperature, dust grains can become larger and gravitationally settle below the photosphere (Allard 1998). Thus, in any attempt to assign effective temperatures to cool photospheres, we must make use of models that take dust formation and behavior into account. Three basic models are considered:

Standard (no-dust) Models: In these models, various molecules are formed with decreasing T_{eff} , but no dust is allowed to form. These are the NextGen series of models described by Hauschildt et al 1999. This scenario is known to be problematic below a certain temperature; Tsuji et al. 1996b have argued that this temperature might be as high as 2800K. A panel of spectra from these models in the Cs I region is shown in Fig. 1, left panel. The opacity is dominated by TiO over most of the spectrum shown. There is also a band due to VO at 8528A ; this is treated with the JOLA (Just Overlapping Line Approximation) method, as no good line lists are available for this molecule. The apparent TiO strengths remain high throughout the temperature range (2500-1600K) shown, and the Cs I line at 8521A grows moderately stronger. It does not achieve anything like the observed strengths of Cs I in L dwarfs.

Dusty Models: Here, various molecules are formed with decreasing T_{eff} , which then coalesce into dust grains that remain in the photosphere. A range of grain sizes is assumed, and the resulting dust opacity taken into account, as well as the photospheric depletion of dust-forming atoms and molecules. These models are described by Leggett et al. 1998 and Allard 1998. The same spectral region as above is shown for this model approximation in Fig. 1, right panel. Even at 2600K the spectrum looks rather different, as Ti is already condensing out and becoming unavailable to the molecular bands. A very different set of molecular lines is apparent at 2200K, and the Cs I line has actually disappeared! This is not due to depletion of atomic cesium, but the growth of stronger opacity sources. At cooler temperatures, all the molecular lines are increasingly weakened by the growing dominance of the (featureless) dust opacity, leaving a rather smooth spectrum by 1600K. What is not apparent from these normalized plots is that the actual flux levels are quite different in the 2 panels. In the models without dust the TiO lines strongly suppress the flux, while the dusty case is brighter not only because of lower opacity but because the atmosphere is heated by absorption of radiation by the dust.

Cleared-Dust Models: In this case as dust grains form they are assumed to gravitationally settle below the photosphere. These models are constructed using the full dust equation of state (thus accounting for photospheric depletion of dust-forming materials) but neglecting dust opacity. [7] In these spectra (Fig. 2, left panel) the strength of both molecular and atomic lines grow at cooler temperatures. Although TiO is gone, it is replaced by other molecular lines, but these are not nearly as strong in absolute opacity. The VO JOLA feature at 8528A grows stronger with cooler temperatures (not seen in the observations).

---

[7]We have chosen the name "cleared-dust" models to denote the absence of dust *opacity* in these models. In the simplest picture, formation of dust coupled with the absence of dust opacity could be accomplished by the gravitational settling of dust below the photosphere. However, other scenarios may be invoked as well; for example, the dust may collect into photospheric clouds with a small covering fraction, or the dust may form very large grains with a small total blocking efficiency. Thus the absence of dust opacity in the photosphere should not necessarily be taken to guarantee the absence of photospheric dust itself.

The Cs I line becomes very strong at cooler temperatures in agreement with observations. The line wings are easily able to overcome the rather weak molecular opacities, and the line is not only deep but broad. These are collisional damping wings. In Fig. 2 (right panel) we show the analogous spectra for the Rb I region. Similar behavior is apparent, except that the molecular opacities are even weaker, and the line comes to completely dominate the spectral region shown by 1600K. This is partly due to the increased abundance of Rb I compared to Cs I . Of course the K I resonance lines are vastly stronger than Rb I (due to its much higher abundance); these lines grow wings which cover more than 100 A. It is the lack of TiO combined with the lack of dust opacities which allow the atomic lines to grow so strong in these models, and they resemble the observations most closely.

Naively, one might have expected the standard models to hold true in our hottest objects, the dusty models in the cooler objects, and the cleared-dust ones in the coolest objects. However, our observations indicate that the "dusty" models are never representative of the optical observations. On the other hand, Leggett et al. 1998 and Goldman et al. 1999 find their best fit to the infrared photometry (color *and* absolute flux) of L and very late M dwarfs with these dusty models. One way of reconciling this disparity is to postulate that gravitational settling depletes dust in the upper photosphere (where the visible spectrum forms), but not in the lower photosphere (where the IR spectrum forms). In reality, formation of dust clouds, dredging up of grains by convection, and various other meteorological phenomena must be modeled for an accurate portrayal of the situation. The spectrum of Gl 229B, for example, shows no indication for dust in its IR spectrum (from 1 to 5 μm; Oppenheimer et al. 1998), but presents evidence of a strong (unidentified) source of opacity in the optical (Golimowski et al. 1998). Very recently, Burrows et al. 1999 have suggested that this opacity could actually be the far wings of the strong alkali resonance lines! In our present early stages of modeling, we expect the three models outlined above to at least bracket the observed spectra.

4. Analysis

In this section, we present a discussion of the adjustments made to the models for purposes of comparison to the data (§4.1), and the model parameters used for profile-fitting (§4.2), particularly the determination of rotational broadening for each star.

4.1. Model Profile Adjustments

The models must first be corrected for rotational broadening effects (see §4.2) through a convolution algorithm. This effect occurs at the star. There is also a finite instrumental resolution in the observations. Thus, the rotationally broadened models were also broadened by Gaussians in accordance with the HIRES resolution of 31000 (this is an unimportant correction for most of the objects, given their high rotational velocities).

In the data, the presence of overlapping molecular lines makes it necessary to renormalize each model with a derived pseudo-continuum (after an initial normalization with the appropriate blackbody spectrum). Derivation of pseudo-continua in the model spectra is complicated by sudden strong breaks which are not apparent in the observed spectra. These are produced by the Just Overlapping Line Approximation (JOLA) method used to treat VO, FeH, CaH, and CaOH bands, for which insufficient parameters are currently available to allow a more accurate handling of the individual molecular lines. In the cleared-dust models the Cs I line occurs outside (i.e., blueward of) the JOLA break region (Fig. 2, left panel), while the Rb I line occurs within a similar JOLA transition (redward of the break, Fig. 2, right panel). Thus, the models compute the Rb I line with a background opacity higher than the real value, and we expect the model Rb I fits to the data to be less accurate than the Cs I fits. This effect becomes smaller as the Rb I line overwhelms the molecular opacities at the coolest temperatures.

We have compensated for the JOLA breaks in the following fashion. For each resonance line, the model spectrum (in the range 8500-8540A for Cs I and 7930-7960A for Rb I) was divided into three sections - one blueward of the JOLA break region (section 1), one redward of it (section 2) and a narrow section over which the break actually occurs (section 3). A polynomial fit is obtained for section 1, after manually discarding strong spectral lines (selected by eye), and section 1 is normalized by this fit. The flux in section 3 is assigned a single value – the average, after normalization, of the 5 redmost points in section 1. Section 2 is then separately normalized with a polynomial fit (again after discarding strong spectral features). The combined effect of these procedures is to artificially remove the JOLA feature and concurrently normalize the model by the pseudo-continuum. Note that these changes do not affect the actual calculation of the spectrum; they are applied post facto primarily for aesthetic reasons. They have the effect of making the entire model spectrum resemble the observations more closely. We emphasize that the fitting we do is only in the line itself, while the normalization procedure affects primarily the spectrum outside the line. It should not affect our best fit parameters.

4.2. Model Parameters

Effective temperature (T_{eff}), surface gravity (g), metallicity ([M/H]) and projected rotational velocity (v sin$i$) are all fundamental parameters which affect the observed spectra. In our case T_{eff} is kept a free parameter. Surface gravity, metallicity and rotational velocity all affect the observed line-broadening. Higher surface gravity increases the pressure at every atmospheric layer, causing increased collisional (Van der Waals) line-broadening, and a larger concentration of molecules at every layer. The net effect is a broadening of the line with increasing gravity (Schweitzer et al. 1996).

Metallicity enters in two opposite ways. First, higher metallicity decreases the proportion of hydrogen particles (which are the main source of collisional broadening). Second, higher metallicity also implies a decrease in pressure at a given optical depth (because of higher opacity), thereby reducing the line-broadening (this second effect probably dominates the first one, unless one goes to extremes of metallicity). The net effect is a narrowing of the line with increasing metallicity (Schweitzer et al. 1996). Higher metallicity also implies a greater abundance of alkali nuclei, which increases the strength of the atomic alkali lines. This effect is diminished to the extent that the alkali metals end up in molecules. Notice that increasing gravity and increasing metallicity affect line-broadening in opposite senses; making the determination of gravity and metallicity a non-trivial task in cool dwarfs. Meanwhile, stellar rotation (corrected for the inclination of the rotation axis) Doppler broadens the line profile, and changes the way it merges into the surrounding pseudo-continuum. In fitting line profiles these various effects must be disentangled as much as possible.

Stellar evolutionary models indicate that late-M and L dwarfs should have a surface gravity given approximately by log[g]=4.5 - 5.5 (Baraffe et al. 1998; Burrows et al. 1997). Ideally one should keep g a free parameter between these limits during profile-fitting. At the time of writing, however, AH cleared-dust models were not yet available for values of log[g] other than 5.0. A subsequent paper will discuss the results of varying g. Similarly, metallicities for these relatively young objects may reasonably be supposed to be solar, but can vary somewhat about this value. In this paper we assume a solar metallicity and defer dealing with metallicity variations.

Finally, though the known rotation velocities of very early M-dwarfs (<M3) is usually $\lesssim$ 5 km s^{-1} , a significant fraction of the mid-M dwarfs (M3.5 - M6) show faster rotation (Delfosse et al. 1998). Moreover, a trend toward increasing rotation velocity has been observed as one moves to later M spectral classes (Basri & Marcy 1995; Basri et al. 1996; Tinney & Reid 1998), so that rotational effects must be considered. For the late M and early L-dwarfs in our sample, v sin$i$ is determined by correlating their spectra in the

interval ∼8630 - 8753A with that of Gl 406 in the same interval. This spectral interval contains molecular lines caused by VO, TiO, CrH and FeH. The v sin$i$ for Gl 406 has been determined by Delfosse et al. (1998) to be < 3 km s^{-1} ; thus it can be considered at the level of accuracy desired here to be non-rotating (since our instrumental broadening is of the same order).

We first obtain the correlation function between our target spectrum and Gl 406 in the specified spectral interval. We then artificially rotate our observed Gl 406 spectrum to various velocities by a convolution algorithm, and obtain the correlation function between each of the rotated Gl 406 spectra and the original unrotated Gl 406 spectrum, in the same spectral interval. Correlation functions are normalized to unity in the "wings", and additively adjusted so the amplitude of the main peaks are matched. The correlation function thus obtained that best matches that between the target object and the unrotated Gl 406 spectrum is selected, and the corresponding rotation velocity assigned to the target object.

A difficulty arises with this procedure for the cooler L dwarfs (later than L1) in our sample. Their spectral features in the chosen interval (or in any other interval available to us) are not very similar to those in Gl 406. New molecular lines appear (as expected) with decreasing T_{eff} , and the correlation function of Gl 406 with the L-dwarfs is no longer similar to those of Gl 406 with rotated versions of itself. To determine the rotational velocities of the cooler L dwarfs, therefore, we have tested two separate and independent methods.

The first of these is to keep the v sin$i$ of the cooler L dwarfs a free parameter during profile fitting, along with the effective temperature. Keeping the rotational velocity a free parameter, of course, introduces some ambiguity into the derived effective temperatures as well. That is to say, models with different effective temperatures fit the same data when different values of v sin$i$ are used.

Luckily the ambiguity is limited in the cleared-dust models. Decreasing T_{eff} increases both line width and line depth, while increasing v sin$i$ also increases line width but decreases line depth. This makes it easier to constrain the model fits to narrow ranges in T_{eff} and v sin$i$. As the temperature becomes very low ($T_{eff} \lesssim$1600K), collisional broadening overwhelms the velocity broadening, and rotational velocity becomes harder to measure through profile fitting at low temperatures. These effects are demonstrated in Fig. 3. On the other hand, the sharpness of the molecular lines is rather insensitive to T_{eff} , even at low temperatures, and very sensitive to rotational velocity. Thus, it is possible to use the sharpness of molecular lines as a diagnostic of v sin$i$. This is not trivial for our sample, mostly because of noise in the data and because the modeling of the individual molecular lines is rather imperfect. However, we find that line width, line depth and molecular lines all considered together do provide tight constraints on the effective temperature and rotational velocity.

Our second method of determining rotational velocities for the cooler L-dwarfs is to use the cross-correlation method described previously, but now using as a calibrator not Gl 406 but an early L-dwarf (whose $v \sin i$ *can* be determined by cross-correlation with Gl 406). However, we face the difficulty that an ideal calibrator, by definition, should be a *non*-rotator, while we have not yet found any non-rotating L-dwarfs. Both G196-3B and 2MASSW 1439+1929, the slowest L-dwarf rotators in our sample, have a $v \sin i$ of 10 km s^{-1} (as determined through cross-correlation with Gl 406). Is it possible to use either of these two objects as calibrator to accurately determine the $v \sin i$ of cooler L-dwarfs? We examine this question in the Appendix, and determine that the calibrator can be rotating, so long as the targets rotate sufficiently faster than the calibrator. Thus, G196-3B or 2MASSW 1439+1929 can be used to derive the rotational velocities of the cooler L-dwarfs, so long as the latter are yet more rapidly rotating objects. More precisely, the cooler L-dwarfs need to be rotating faster than 30 km s^{-1} for their $v \sin i$ to be determined precisely, without any correction factors, by cross-correlation with G196-3B or 2MASSW 1439+1929. If the cooler L-dwarfs have vsini between 10 and 30 km s^{-1} , their rotational velocities can still be precisely determined through cross-correlation with G196-3B or 2MASSW 1439+1929, after applying a small correction factor of $\lesssim$ 5 km s^{-1} (see Appendix for a discussion of this).

From the profile fitting method discussed above, we find that the cooler L-dwarfs in our sample all have vsini $\gtrsim$ 20 km s^{-1} , with an error of $<$ 10 km s^{-1} ; i.e., all the cooler L-dwarfs are rotating faster than G196-3B and 2MASSW 1439+1929. Thus, it is possible to determine their vsini precisely using either G196-3B or 2MASSW 1439+1929 as calibrator (see Appendix). We choose 2MASSW 1439+1929 as our calibrator, since it appears, from our model fits in Cesium and Rubidium, to be slightly cooler than G196-3B, and should thus be spectrally more similar to the later L-dwarfs, resulting in more robust correlation functions.

We must also ask whether collisional broadening, due to surface gravity or metallicity variations, could affect our correlation method results by providing broadening we mistake as rotation. Models with different metallicities have not yet been produced, but “no-dust” (NextGen) AH models with different gravities are available. By rotating models with different gravities ($\log[g]$ = 3.5, 4.5, 5.5) to various velocities and cross-correlating between them, we find that the cross-correlation function is insensitive to gravity, even over the large range of gravities considered. Thus, the $v \sin i$ we derive are likely valid even if our sample objects do not have our assumed value of log[g]=5.0. Insofar as metallicity effects are comparable to gravitational ones, the same should hold true for them. In the end, we find the cross-correlation method to be both a more precise and reliable means of setting $v \sin i$, and adopt it hereafter. This allows us to determine temperatures below

5. Results

5.1. The L Spectral Class

Using information on the effective temperatures found below which best fit our profiles, Martín et al. 1999b have assigned subclasses to the L-type objects in our sample based on low dispersion spectral indices. They propose a subclass designation similar but not identical to that proposed by Kirkpatrick et al. 1999a. Hotter objects have with the same classifications, but the scale extends to L6 rather than L8 for the range of known objects. We argue here that because of the temperature range we infer for our sample, it seems preferable that the L spectral range not be "used up" by the current sample.

A good compilation of the temperature scale for spectral classes can be found in deJager & Nieuwenhuijzen 1987. The temperature ranges spanned by the traditional spectral classes are not uniform (reflecting historical ignorance and old observing techniques, as well as diverse effects of temperature on the appearance of spectra in different ranges). The OB spectral classes cover large ($>$ 10000K) temperature ranges. The A class covers almost 3000K, and the rest are between 1000K and 1500K (the shortest range is for G stars). The M stars span a range of 1500K. If the coolest currently known L stars are classified L8 (as in the Kirkpatrick et al. 1999a scheme), we find that the L spectral class would cover a significantly smaller range of temperatures (600K) than any other spectral class. The spectral differences between some of the Kirkpatrick et al. 1999a subclasses are also rather subtle.

Where to place the cool end of the L class is not obvious from spectral considerations (the hot end is dictated by the already defined M subclasses). The main optical/NIR spectral characteristics of L stars are the dominance of hydrated molecules and the neutral alkali atomic lines. The Cs I lines are still visible in Gl 229B, and Burrows et al. 1999 have argued that the sodium and potassium line wings are a dominant opacity source in the optical spectra of similar objects. The conversion of CO to CH_4 is similar to the conversion of other oxides to hydrides which happens at the beginning of the L class. Nonetheless, the community seems agreed that Gl 229B (a "methane dwarf") deserves yet another spectral class. Kirkpatrick has suggested "T" and this has already has received some usage; Martín et al. 1999b propose "H". We do not know how close the coolest currently known L dwarfs are to showing methane, nor does the appearance of methane logically terminate the L spectral class. Indeed, the appearance of methane depends on which band one is talking about. The strongest (but observationally more difficult) 3.5 micron band is predicted to appear at about the temperature of our coolest objects. The 2 micron bands seen in Gl 229B probably appear below 1500K and become very strong by 1000K, where the optical bands are just becoming visible.

The proposed subclass scale for the L spectral class in Martín et al. 1999b has a direct physical basis. They propose that it begin at 2200K, and that each subclass be 100K cooler than the last. While spectral classification schemes historically have not explicitly considered the physical temperatures of the objects, there is no compelling reason to continue that practice in the new millennium. Martín et al. 1999b show that their scheme is compatible with the apparent changes in low resolution spectra, and with the color variations of the objects. It is possible that there will be an absolute shift (probably downward) in the whole scale when the dust and molecules are treated more accurately. It is also possible that refinements in the translation of spectral diagnostics to temperature would cause some of the preliminary designations in either classification paper to be modified again in the future.

We note that our modification to the Kirkpatrick et al. 1999a scale is actually rather mild in principle. They thought that their L8 object (2MASSW 1632+1904) might have a temperature as low as 1400K, and we would similarly assign L8 to 1400K. The main disagreement is that we find this object to be more like 1700K (which should be L5 in the temperature-based classification scheme). Our preliminary temperature for DENIS-P J0255-4700 (which appears to be slightly cooler than 2MASSW 1632+1904) was 1600K, which led to the Martín et al. 1999b classification of L6 (here we finally settle on 1700K). Of course, we do not claim that the temperatures found here are the final word. The community will have to reach consensus on the L classification scheme after a full range of ultra-cool objects is discovered and studied in both the CCD and near-IR spectral ranges, and a final temperature determination for them is found.

In Table 2 we provide a summary of our results. The spectral types listed are from Martín et al. 1999b for the objects common to both our samples. In most cases, their spectral classification agrees with our T_{eff} determinations. In the case of DENIS-P J1208+0149, however, Martín et al. 1999b find M9, while our Cs I T_{eff} indicates a somewhat later spectral type (∼M9.5). Martín et al. 1999b also assign L6 to DENIS-P J0255-4700 and 2MASSW 1632+1904, while our T_{eff} determination suggests a slightly earlier type (∼L5-5.5). 2MASSW 1146+2230, 2MASSW 1439+1929, DENIS-P J0021-4244 and DENIS-P J2146-2153 are not included in the Martín et al. 1999b sample. In the cases of 2MASSW 1146+2230 and 2MASSW 1439+1929, therefore, the listed spectral types are from Kirkpatrick et al. 1999a, since they are consistent with our T_{eff} determination. DENIS-P J0021-4244 and DENIS-P J2146-2153 are not in the Kirkpatrick et al. 1999a sample either, so we assign a spectral type to them based on our derived T_{eff} for the two objects and the spectral type given by Martín et al. 1999b for objects with similar T_{eff} .

5.2. General Considerations for Profile Fitting

Our preliminary profile-fitting of both the Cs I and Rb I lines indicates that the cleared-dust models are the only ones that fit the entire line data set well. The dusty models do not agree with the data – dust opacity in the models makes the lines much weaker than observed. The no-dust models do not fit most of the data either, producing lines that are much narrower than those actually seen when the line depth is approximately correct, even after reasonable rotational broadening. This is because in the no-dust models, the opacity in the wings of the resonance line is dominated by molecular opacity rather than the line wing opacity itself; hence only the narrow core of the resonance line is visible.

When no-dust models do fit the data, the inferred temperatures (2400-2700K) agree with those from cleared-dust model fits. Moreover, these inferred temperatures are high enough that we expect dust formation to be relatively unimportant; the no-dust and cleared-dust models should resemble each other. In short, we found that cleared-dust models always produced fits at least as good as, and mostly much better than, either of the other two model types. This is in agreement with the conclusions of Tinney et al. 1998, who finds that cleared-dust models provide the best overall spectral shape fits in the optical regime for their sample of DENIS objects. In what follows, therefore, we only consider the results of profile fitting with cleared-dust models. We note again that in the infrared, dusty models do a better job of fitting SEDs (eg. Leggett et al. 1998). The left panels of the remaining Figures show the best fits for Cs I and the right panels show the best fits for Rb I . When looking at the observed molecular regions, it may appear that the expected smoothing with increasing rotation is not present. This is because the spectra are somewhat noisy, and noise spikes have the same “sharpness” regardless of rotation. The eye is fooled by this, but a cross-correlation function is not.

Before going on to examine the results of profile-fitting for each of the objects in detail, certain general comments can be made. First, the selection of best fits has been done by eye; any quantitative fitting procedure would, in our opinion, require more accurate synthetic spectra (especially for the molecular lines) and less noisy observations than are currently available. Second, the figures show both data and models after smoothing with a 5-pixel box; this was done to allow the eye to follow the fit better by reducing noise fluctuations; a 5-pixel box, applied to the models and our current data sample, does this well without affecting the integrity of the resonance line significantly. However, the actual model fits were derived by comparing unsmoothed data and models, to eliminate the possibility of overlooking real but sharp features during profile fitting. This is important for two reasons. First, the very core of the data is sometimes chopped by noise, and so the real depth of the line may be represented by very few pixels, less than in the noise-free model. In this case, smoothing alters the depth of the data to a larger extent than that of the model. More importantly, there appear to be real molecular features within the wings of the Cs I and Rb I resonance lines that are not present in the models. Smoothing before profile fitting causes these lines to blend into the observed resonance line and make the resonance line broader than would be caused by smoothing alone. Since these molecular features are unmodeled (or insufficiently modeled), a similar effect does not occur when the models are smoothed. Thus, a broader model must be chosen to fit the data than would be necessary if no smoothing were performed, leading to derived effective temperatures that are artificially lower. Therefore, profile fitting was done with unsmoothed data. Where unmodeled molecular lines are present within the observed resonance lines, the fit was obtained to the resonance line alone, after excluding (by eye) the molecular lines.

Finally, there exist certain obvious general discrepancies between the models and the observed spectra, which are better noted at the outset rather than repeatedly on an object-by-object basis. The first of these are the poorly modeled or unmodeled molecular lines mentioned above, that appear in the wings of the Cs I and Rb I resonance lines. They are obvious in the unsmoothed data, and appear in the smoothed data as discontinuous broadenings in the Cs I and Rb I line wings (see for example the Cs I and Rb I fits to Kelu-1 (Fig. 13)). In general, they appear to increase in number and strength with decreasing T_{eff} . This is expected, as the resonance line wings become broader with decreasing T_{eff} and include increasing numbers of the continuum molecular lines. Hence, since the models do not exactly reproduce the observed continuum molecular lines, they also do not accurately reproduce the observed resonance lines at lower temperatures. On the other hand, the rotational velocity of the objects also increases with decreasing T_{eff} , which smooths out the molecular lines more than it does the stronger resonance lines. At a given T_{eff} , therefore, this allows better model fits to the data with increasing $v \sin i$ (compare the 25 km s^{-1} , 2200K Cs I fit to DENIS-P J0909-0658 (Fig. 10), to the 10 km s^{-1} , 2200K Cs I fit to DENIS-P J2146-2153 (Fig. 9)). Of course, some of the features within the resonance lines may simply be noise spikes and not real molecular lines, especially in our low S/N observations (e.g., Rb I spectrum of DENIS-P J1228-1547 (Fig. 17)). However, this is not likely to be the case for those features that repeatedly appear in the spectra of a number of different objects.

Furthermore, for Rb I , there is a break in the observed spectra at $\sim$ 7939A that is not reproduced in the models; the lack of agreement between models and data is most pronounced for this feature in the Rb I temperature range $\sim$ 2300-2700K (2MASSW 1439+1929 to Gl 406). This feature, in fact, looks somewhat like the JOLA break that we labored to remove from the models. However, a comparison between the uncorrected models (Fig. 2, right panel) and the data in the 7930-7960A range shows that the observed feature occurs blueward of the JOLA break in the models, and is stronger than the JOLA breaks at the same temperature. Also, the observed opacity break is limited to only a small span of wavelengths; this is not true for the modeled JOLA breaks, which persist over large wavelength spans. Only in LP 944-20 (Fig. 6, right panel) does the observed opacity break resemble the (removed) JOLA break. Finally, the model JOLA break persists to much lower temperatures than the observed feature. Thus, even if this is the feature that the JOLA formulation tries to simulate, the simulation is not a good one. Except for this particular feature, there is reasonable agreement between the models and the data in the 7930-7960A range after the model JOLA break has been corrected for, so we appear vindicated in making this correction.

The effect of the JOLA break on the fine analysis is complicated. On the one hand, the extra background opacity will tend to make the line look weaker (similar to the effect of dust in the "dusty" models). This would require a cooler model to reproduce a given observed line strength, since the line grows with decreasing temperature. On the other hand, the effect of the JOLA break can be reduced by making the model hotter (which lets the model line appear stronger). The question is whether this reduction goes faster than the reduction in line strength caused by the hotter temperature. Our actual results suggest that it does, which leads us to derive generally hotter temperatures from the Rb I line than the Cs I line.

For Cs I , there is an absorption line, centered on $\sim$8514A , that appears in the models but is absent in the data. This feature becomes weaker with decreasing effective temperature. There is also a molecular feature at $\sim$ 8505A , that becomes stronger with decreasing temperature in the models but follows the opposite trend in the data. This leads to poor agreement between models and data at this wavelength at effective temperatures below $\sim$2000K.

There are other small anomalies in the Cs I region. In all but one of the observed objects with Cs I T_{eff} between 2150 and 2800K (2MASSW 1439+1929 to Gl 406, except DENIS-P J1208+0149), there appear to be molecular bands (not strong in the models) at 8506 and 8516A; the latter impinges on the Cs I line. Thus, when the normalized models and data are overlaid, the models appear brighter than the data over this wavelength range. To correct for this, the models (for only the objects indicated above) were also renormalized so as to fit the data between 8516 to 8524A. We show both normalizations in the figures for these objects, and tended to choose the temperature which fit the Cs I line as normalized near it. It is conceivable that this molecular band is the one that the model JOLA breaks try to simulate, but if so, the simulation is an inadequate one, for much the same reasons given above for the feature at 7939A. It is worth noting that both features occur over the same temperature range, and might thus be caused by the same molecule, VO or TiO.

Finally, a note about which model fits are given, and why. For spectra for which only a single model is given, no other model was found to reasonably fit the data. Where two model fits are given, confusion between noise and unmodeled molecular lines within the resonance line precluded a more accurate fit. If the lines within the observed resonance line are noise spikes, then the correct model fit should 'average' them out (run through them), while if they are truly unmodeled molecular lines, then the model fit should exclude them altogether. In general, we have treated lines that appear repeatedly in the spectra of different objects, and/or are strong (deeper and broader than average noise spikes) as molecular lines, and the others as ambiguous (i.e., leading to more than one model fit).

As noted previously, the figures show the models and data smoothed by a 5-pixel box. In cases where blending of unmodeled molecular lines makes the smoothed data appear much broader than the purported model fits, we also show the unsmoothed data, to indicate the excluded molecular lines and support our model fit. Since, as mentioned before, the smoothing does not alter the models to any appreciable degree (unlike the data), it is justifiable in these figures to compare the unsmoothed data to the smoothed models (though the actual profile fitting has been done more accurately by comparing unsmoothed models with unsmoothed data).

5.3. Gl 406 (M6V)

Delfosse et al. 1998 find a $v \sin i$ of <3 km s^{-1} for Gl 406; at our level of accuracy, this is indistinguishable from no rotation at all. With $v \sin i = 0$ km s^{-1} , we find $T_{eff} = 2800$K from the Cs I cleared-dust model fits and 2700K from the Rb I , in agreement with the result of Jones et al. 1994. The 2800K model Cs I line is slightly shallower than what is observed (Fig. 4) but otherwise fits the line wings and core well. The molecular lines near the resonance line are reasonably well fit after renormalization, while the fit to the molecular lines further away is good before renormalization. The model Rb I line fits the observed line core and wings well, except in the partially modeled molecular feature in the right wing. The molecular lines are also fit, and there is no significant worsening of the fit as one moves away from the line over the wavelength range considered here. It is noteworthy that this is the only object in our sample for which we derive a Cs I T_{eff} that is higher than the Rb I one; in all our other objects, the Cs I T_{eff} is lower than the Rb I .

5.4. LHS 2924 (M9V)

We derive a rotational velocity of 10 km s^{-1} . An effective temperature of 2400-2500K is derived from the Cs I fit, and 2600K from the Rb I fit; these values are somewhat higher than the ∼2200K found by Jones et al. 1994 from a low-resolution IR spectrum. In both cases the line core and wings are fit very well (Fig. 5). In Cesium, the molecular lines near the resonance line fit well after renormalization, while the lines further away match better before renormalization. The higher flux in the model on the right edge of the Cs I line is caused by smoothing; the right edge in the unsmoothed data matches the model well. The partially modeled molecular lines are evident in the wings of the Rb I line, but the overall fit to the molecular lines is good in Rubidium.

The effective temperature scale for late-M dwarfs is in fact still under discussion. These objects may be, in some ways, more sensitive to the treatment of dust than the L dwarfs (for which ignoring dust opacities altogether seems to work). We have a large sample of other late-M spectra, and will revisit this question in a subsequent paper (with updated AH models). The several objects listed as M9.5 below do not have exactly the same temperatures.

5.5. LP 944-20 (M9.5V)

This is a confirmed brown dwarf, with a mass between 0.056 and 0.064 $M_{\odot}$, aged between 475 and 650Myr (Tinney 1998). We derive a rotational velocity of 30 ± 2.5 km s^{-1} which agrees with Tinney & Reid 1998. The Cs I fit gives T_{eff} =2400K and the Rb I fit gives T_{eff} =2600K. Kirkpatrick et al. 1997 assign a spectral type of $\gtrsim$ M9V to LP 944-20, similar to LHS 2924 (M9V). We find it marginally cooler than LHS 2924, at least as implied by the cesium fit. In both Cs I and Rb I , the models fit the line core and wings well (Fig. 6), and the nearby molecular lines moderately well. The higher rotational velocity smooths the model molecular lines to a degree comparable to that observed, but there is poor agreement between individual lines in the models and the data.

5.6. DENIS-P J0021-4244 (M9.5V)

We obtain a $v \sin i$ of 17.5±2.5 km s^{-1} for this object. The Cs I fit yields an effective temperature of 2300K, and the Rb I fit an effective temperature of 2400-2500K. The resonance lines in both cases are fairly well fit (Fig. 7), with the data being slightly wider than the models in the wings, due to poorly modeled molecular lines. In Rb I , the 2400K model is a little deeper than the data and overestimates the width of the line by fitting the unmodeled molecular line on the right, while the 2500K line matches the true width of the line but is somewhat shallower than the (unsmoothed) data. The nearby molecular lines are well modeled in the Rb I section (at least in shape, if not in depth) and somewhat less so in the Cs I . The lines further away from the resonance line are well reproduced in the Cs I section before renormalization. The TiO features in this object are quite similar to those of BRI 0021 (M9.5).

5.7. DENIS-P J1208+0149 (M9V)

We derive $v \sin i = 10$ km s^{-1} for DENIS-P J1208+0149, through cross-correlation with Gl 406. An effective temperature of 2200-2300K is found from the Cs I fits, and of 2500K from the Rb I fits. The Rb I fit is good, except for the unmodeled molecular lines in the wings. The fit to the molecular continuum in this spectrum is good as well. In Cs I , the line core is fit well by the 2200 and 2300K models (though the former is slightly broader and the latter a little shallower than the unsmoothed data), but both models appear much stronger than the data at the edges of the smoothed resonance line. However, the models match the unsmoothed data well at the edges.

Our results are slightly puzzling. Martín et al. 1999b find this object to be of spectral class M9, while our Cs I T_{eff} puts it at $\sim$ M9.5. However, our Rb I T_{eff} , which agrees with the Cs I T_{eff} ordering for most of the objects in our sample, does not in this case but implies instead that the object is somewhat hotter than 2200-2300K. Unfortunately, we do not have color data for this object. The opacity band over 8516-8524A which is apparent in all other objects in the temperature range 2150-2800 K is not seen in this object. These anomalies may result from the noisiness of the data. This will have to be resolved with better spectra and improved models.

5.8. DENIS-P J2146-2153 (L0)

We find a rotational velocity of 10 $\pm$ 2.5 km s^{-1} for DENIS-PJ2146-2153. An effective temperature of 2200K is derived from the Cs I fit and of 2400K from the Rb I fit. In the Cs I section, the inclusion of unmodeled molecular lines makes the smoothed resonance line appear inordinately broad in the wings, but a good fit is obtained to the unsmoothed data after excluding the molecular lines. The Rb I resonance line is well modeled, though the data is slightly broader than the model in the left wing, due to a partially modeled molecular line (Fig. 9). Both models are good fits to the continuum molecular lines, the Cesium models slightly better so before renormalization than after.

We also note that while we assign this object to class L0, the low resolution spectrum of Tinney et al. 1998 indicates M9; in particular, at low-resolution this object appears hotter than BRI 0021 (M9.5+). A comparison of the TiO features in our spectra with a HIRES spectrum of that object bears this out. We need the Cs I spectrum of BRI 0021 to sort this out; our Rb I line here is stronger than that reported for BRI 0021 by Basri & Marcy 1995.

5.9. DENIS-P J0909-0658 (L0)

We obtain a rotational velocity of 25$\pm$2.5 km s^{-1} for this object. An effective temperature of 2200K is derived from the Cs I fit, and 2400K from the Rb I fit. In both cases, the line core and wings are well simulated by the models (Fig. 10), except a poorly modeled molecular line in the right Rb I wing. The Cs I line does not show any evidence of unmodeled molecular lines; this may be a result of this object's higher $v \sin i$, which would tend to smooth out such lines, or the fact that the previously unmodeled molecular line has disappeared with decreasing T_{eff} . The former explanation would seem to be the more correct one, since 2MASSW 1439+1929, which we find (see below) has a very similar Cs I T_{eff} ($\sim$2150K) but is a slower rotator (10 km s^{-1}) does show evidence for unmodeled lines in Cs I .

Nearby molecular lines are fit well in the Cs I section, and poorly in the Rb I section, which appears noisier than the Cs I section. The low resolution spectra of this object also suggest it is a good marker of the start of the L spectral type (Martín et al. 1999b).

5.10. G196-3B (L1:)

This substellar object was recently discovered by direct imaging (Rebolo et al. 1998), at a distance of $\sim$ 300 AU around the young low-mass star G196-3 (M3Ve). Its mass has been determined to be 25 (+15/-10) M_J and its age to be $\sim$ 100Myr (from the activity level of the primary star). By comparing low-resolution spectra of G196-3B with those of Kelu-1 and DENIS objects, Rebolo et al. infer an effective temperature of 1800-2000K.

We derive a rotational velocity of 10$\pm$2.5 km s^{-1} for G196-3B using Gl 406 as calibrator. This is relatively slow at such low mass, especially for such a young object (however, this may be simply a projection effect). This gives us an effective temperature of 2200K from the Cs I model fit and 2400K from the Rb I fit. The fit in Cs I is good in the line core and wings. The increased model flux on the right edge of the Cs I line is an effect of smoothing; the unsmoothed data matched the model right edge well. The overall fit to the molecular lines in the Cesium section is good before renormalization. The model Rb I line is slightly deeper than the data after smoothing, but matches the unsmoothed data well. It is also slightly narrower than the observation in the wings due to poorly modeled molecular lines. The overall fit to the molecular lines is good in the Rubidium section, though the data appears somewhat noisy.

Our derived T_{eff} is higher than Rebolo et al.'s estimate. However, the molecular band between 8516A and 8524A that is present in all other objects in our sample that have $T_{eff} \gtrsim$ 2200K, is present in G196-3B as well, giving credence to our higher temperature estimate. On the other hand, the low-resolution spectrum obtained by Rebolo et al shows a clear lack of TiO bands and only a very faint VO band, indicating that this is an early L class object.

Our high effective temperature might be due to effects of low surface gravity. Given the apparent youth of G196-3B, it is reasonable that the object is still contracting. A perusal of no-dust AH models at various gravities in the temperature range 2600-3200K shows that the Rb I line is unable to distinguish between low gravity/low T_{eff} and high gravity/high T_{eff} environments, which would explain our good Rb I fit. However, these same models indicate that no such confusion exists in the Cs I line in the 2600-3200K range, in which case we cannot explain our present good Cs I fit if indeed G196-3B has a low surface gravity. It may be, however, that the Cs I line shows behavior analogous to the Rb I at temperatures lower than 2600K, which are not explored in the present no-dust AH models. This question will have to be examined in the future with newer models. Since the no-dust AH models also indicate that the TiO band ($\sim$7040-7140A) is relatively insensitive to gravity but sensitive to temperature, it may also be useful in separating gravity and temperature effects in G196-3B.

5.11. 2MASSW 1439+1929 (L1)

This is a very high proper motion object, at a distance of ∼15.1 pc (Kirkpatrick et al. 1999a). We find a rotational velocity of 10±2.5 km s^{-1} for this object through cross-correlation with Gl 406. The cross-correlation function was checked against that obtained for G196-3B - since both objects are found to have v sin$i$ of 10 km s^{-1} through cross-correlation with Gl 406, and are of similar spectral type, their correlation functions with Gl 406 should be identical - and v sin$i$ sim 10 km s^{-1} was confirmed. This object was subsequently used as a calibrator for deriving the radial and rotational velocities of all the later L dwarfs in our sample.

The Cs I model fits imply an effective temperature of 2100-2200K for this 2MASSW 1439+1929, and the Rb I fits 2300K. Both 2100 and 2200K models are slightly narrower than the data in the red wing of Cs I , because of unmodeled molecular lines. The 2100K model also seems to reproduce the molecular line in the blue wing, but is slightly deeper than even the unsmoothed data, while the 2300K model does does not reproduce the observed blue wing as well, but matches the core depth better. The molecular lines near the Cs I line are reasonably matched by both models after renormalization, and the general molecular continuum well fit before renormalization. This is the coolest object in which the anomalous opacity band between 8516-8524A is seen. In the Rubidium section, the model is slightly narrower than the observed Rb I line due to unmodeled molecular lines, and the continuum is generally well matched in shape but not strength. Our spectral classification of 2MASSW 1439+1929 as L1 agrees with result of Kirkpatrick et al. 1999a.

5.12. Kelu-1 (L2)

Kelu-1 is a free-floating brown dwarf (Ruiz et al. 1997) at a distance of ∼ 20pc (Ruiz: priv. comm.). A rotational velocity of 60±5 km s^{-1} is derived using 2MASSW 1439+1929 as calibrator. From the Cs I fits an effective temperature of 2000K, and from the Rb I fits, a temperature of 2200K are found. In Cs I , the inclusion of poorly modeled lines makes the smoothed data appear much broader than the model, but the fit to the unsmoothed data is good. In Rb I , again, the smoothed data appears much broader than the model, but the 2400K model fit matches the unsmoothed data well. The cores of the observed Cs I and Rb I lines appear to be somewhat chopped by noise.

Our derived rotational velocity for Kelu-1 is very high, even given the trend towards increasing rotational velocity as one moves to the bottom of the main sequence (Basri et al. 1996). Presumably we are near its equatorial plane. In both Cs I and Rb I , the models match the overall observed smoothness of the molecular lines, lending credence to our high derived $v\ \sin i$, but do not match the lines in detail. If indeed our derived T_{eff} (which is dependent on our derived $v\ \sin i$) for Kelu-1 is correct, then we find it to be cooler than 2MASSW 1439+1929 but hotter than 2MASSW 1146+2230, which is in agreement with the results of Kirkpatrick et al. 1999a. Moreover, Ruiz et al. 1997 find that the best fit to the Kelu-1 spectral energy distribution is given by a dusty AH model with T_{eff} = 1900 ± 100 K and log[g] = 5.0 - 5.5 (with [M/H] fixed at 0.0). Leggett et al. 1998 find a best fit to the Kelu-1 IR colors (using AH dusty models) at $T_{eff} \lesssim 2000$K, and [M/H] = 0.0 (holding log[g] fixed at 5.0). Together, the two studies suggest that log[g] = 5.0-5.5 and [M/H] $\sim$ 0.0, consistent with the values we have chosen, are suitable choices for Kelu-1, and that our T_{eff} is also in the right ballpark (perhaps a little hot). Taken together, this again suggests that our $v\ \sin i$ is also approximately correct.

One implication of such a high $v\ \sin i$ is that spectra with an exposure time of an hour or more actually sample most of the stellar surface. Searches for variability or "weather" on this object, must therefore be done using short exposures (forcing low spectral resolution). The rapid rotation may well be the explanation for the rather different equivalent widths reported by different authors (Rebolo et al. 1998). The rotation means that the pseudo-continuum will be set somewhat differently at low, medium, and high spectral resolutions. In fact, we now have high resolution spectra of Kelu-1 from 4 separate nights spanning a year (2 pairs), and see no evidence of variability in the line profiles.

5.13. DENIS-P J1058-1548 (L2.5)

A corrected rotational velocity of 37.5±2.5 km s^{-1} is obtained by correlation with 2MASSW 1439+1929. An effective temperature of 1900-2000K is derived from the Cs I fit, and of 2000K from the Rb I fit, in agreement with the value ($\sim$ 2000K) derived by Leggett et al. 1998 from infrared photometry for [M/H]=0.0. In Cs I , the 1900K model matches the wings of the line but is slightly deeper than the data, and the 2000K model matches the depth of the line but is slightly narrower than the data (Fig. 14). In Rb I , the model is both slightly deeper and narrower than the data; the unsmoothed data indicates that this is due to a core that is chopped by noise and poorly modeled lines in the wings. The pseudo-continuum is not as smooth as the models, perhaps because of noisy data.

5.14. 2MASSW 1146+2230 (L3)

This object is a close double (separation ∼1”); an LRIS spectrum reveals the companion to be a background star of much earlier type (Kirkpatrick et al. 1999a). 2MASSW 1146+2230 shows a strong lithium line with an equivalent width of 5.1A (Kirkpatrick et al. 1999a). We derive a $v \sin i$ of 32.5±2.5 km s^{-1} for this object through cross-correlation with 2MASSW 1439+1929. The Cs I model fits give a T_{eff} of 1900-2000K, while the Rb I fits give 2100K. The observed spectrum appears noisy, and the models match the general trend but not the observed sharpness of the continuum lines in both the Cesium and Rubidium sections. The Cs I line is chopped in the very core by noise.

This is one of our only objects in which the ordering implied by the T_{eff} from Rb I fits does not agree with that implied by the T_{eff} from Cs I . The Rb I fits imply that 2MASSW 1146+2230 is slightly hotter than DENIS-P J1058-1548, while th Cs I fits imply that it is slightly cooler. However, the two objects are very close in spectral type and $v \sin i$, so, given the noise in our spectra, this does not constitute a serious anomaly. If we follow our convention of giving the T_{eff} derived from Cs I more weight than that from Rb I , we find 2MASSW 1146+2230 to be of spectral type L3, in agreement with the result of Kirkpatrick et al. 1999a.

5.15. LHS 102B (L4)

LHS 102B is an L dwarf proper motion companion to LHS 102 (GJ 1001), a field mid-M dwarf. It was very recently discovered in the course of the EROS 2 proper motion survey (Goldman et al. 1999). The rotational velocity of this object is found to be 32.5±2.5 km s^{-1} , from cross-correlation with 2MASSW 1439+1929. From Cs I model fits, we find a T_{eff} of 1800-1900K and from Rb I 1900K. In both Cs I and Rb I , the resonance lines are well modeled (Fig. 16), though the models are slightly narrower than the data, because of poorly modeled molecular lines. The Cs I fit is also somewhat deeper than the data. The overall fit to the molecular lines is better in Cesium than in Rubidium; in both cases (though more so in Rubidium) the model continuum is smoother than the data, probably due to noisy data. This object is similar to GD165B in general appearance. It shares with GD165B an ambiguity about whether it is really a brown dwarf. While the lithium test has not been applied to GD165B (Kirkpatrick et al. 1999b have argued persuasively that it will fail); LHS102B definitely fails the lithium test. This does not mean that either object is stellar – only that they are older than about 200Myr and greater in mass than 60 M_J . It is likely that objects at about this temperature are near the minimum main sequence temperature. When the L subclass of the minimum main sequence temperature is precisely identified, all cooler objects can safely be certified as brown dwarfs without regard to the lithium test.

5.16. DENIS-P J1228-1547 (L4.5)

This was the second field brown dwarf to be confirmed by the lithium test (Martín et al. 1997). The corrected rotational velocity for this object was found to be $\sim$22$\pm$2.5 km s^{-1} through cross-correlation with 2MASSW 1439+1929. From Cs I model fits, a T_{eff} of 1800K is found, and from Rb I fits, 1900K. However, the Rb I data is very noisy, and thus the effective temperature derived from it is rather approximate. The Cs I line is well modeled (Fig. 17), but the model is slightly narrower than the data in the wings, due to poorly modeled molecular lines, and the data is chopped in the very core by noise. The continuum in the Cesium data also appears rather noisy, and does not match the model smoothness. However, recently Martín et al. 1999a have found that this object is actually a binary (separation 0.3 arcsec), with nearly equal brightness. It may be that one brown dwarf is slightly cooler than the other, in which case we are looking at a composite spectrum, and the issues of line-width and noisiness just mentioned will have to be reexamined after taking binarity into account. Leggett et al. 1998 derive an approximate effective temperature of 2000K (with [M/H]=0.0) for DENIS-P J1228-1547 from infrared photometry, and find it to be cooler than DENIS-P J1058-1548, in agreement with our results (and that of Tokunaga & Kobayashi 1999).

5.17. DENIS-P J0205-1159 (L5)

A corrected rotational velocity of $\sim$22$\pm$2.5 km s^{-1} was derived for DENIS-P J0205-1159 through cross-correlation method with 2MASSW 1439+1929. From the Cs I fits we get a T_{eff} of 1700-1800K. The noisiness of the Rb I data precluded diagnostic profile-fitting to the Rb I line; however, the 1700K model generally matches the form of the data. The Cs I line is well modeled, though somewhat noisy as well - the very core of the line appears chopped by noise , and the molecular continuum in the data does not match the model smoothness (Fig. 18). Unmodeled features in the wings of the observed Cs I line may be due to noise or poorly modeled molecular lines. Both models exclude the apparently real molecular line in the right wing, but the 1700K model fit assumes that the features in the left wing are noise, while the 1800K fit assumes that they are real and thus excludes them completely. The unsmoothed data, being noisy, cannot distinguish between the two.

Leggett et al. 1998 use infrared photometry to propose an effective temperature of ∼ 2000K, which is higher than our result. More discrepantly, they find it to be hotter than both DENIS-P J1228-1547 and DENIS-P J1058-1548, which is at definitely at odds with our results. Tinney et al. 1998 and Delfosse et al. 1999, on the other hand, find the same ordering in temperature based on low dispersion spectra as we do. Tokunaga & Kobayashi 1999 find the same from moderate resolution K band spectra (and a new proposed K color index diagnostic ratio). These discrepancies show why it is valuable to have several independent temperature calibration methods. We suspect this object is cool enough to be classified as a brown dwarf on that basis alone.

5.18. 2MASSW 1632+1904 (L6)

2MASSW 1632+1904 is the coolest L dwarf in Kirkpatrick et al. 1999a, and they find a possible lithium line at their detection limit (EW $\leq$ 9.4A). We do not have the lithium line in our observations of this object. We derive a $v\,\sin i$ of 30±2.5 km s^{-1} for this object through cross-correlation with 2MASSW 1439+1929.

Our spectrum for this object is noisy. From the Cs I model fits we derive an effective temperature of ∼1700K. The model matches the general trend but not the sharpness of the lines in the noisy continuum. In the Rubidium section, the noisiness of the data precluded any accurate fits, but both 1600 and 1700K models appear to follow the general shape of the Rb I line.

Martín et al. 1999b ascribe a spectral type of L6 to this object; we have adopted this since it is consistent with our T_{eff} determination. Kirkpatrick et al. 1999a, on the other hand, classify this object as L8. It is to be noted, however, that they correspondingly believe it to have a T_{eff} of ∼1400-1500K. A T_{eff} of ∼1600-1700K, as we find, would be more appropriate to ∼L6-5 in their classification scheme as well (if it were temperature rather than spectral feature based).If our temperature is right, they may wish to consider their translation of spectral features to L subclasses.

5.19. DENIS-P J0255-4700 (L6)

This is our object with the strongest Cs I line, so we think it is the coolest of the sample. For this object the rotational velocity was found to be 40±2.5 km s^{-1} by cross-correlation with 2MASSW 1439+1929. From Cs I model fits, we find a T_{eff} of 1700K, and from Rb I , 1900K. In Cs I , the inclusion of unmodeled molecular lines makes the smoothed data appear much broader than the model, but the unsmoothed data fits the model well. The observed molecular continuum appears somewhat noisy, but seems to match the overall smoothness of the models. The Rb I data is noisy, but the resonance line is reasonably fit by both 1900K after excluding the unmodeled molecular lines.

Despite the fact that it does not show lithium, it is very likely a brown dwarf based on its Cs I temperature (with mass greater than 60 M_J). Griffith et al. 1998 worry about whether lithium may not show up due to formation of molecules such as LiCl, but this object is not too much cooler than DENIS-P J1228-1547 (which shows lithium). Even more reassuring is the detection of lithium in some objects this cool by Kirkpatrick et al. 1999a, although they do see a possible beginning of the expected weakening of lithium at very cool temperatures. The results of Griffith et al. 1998 are suspect, since they have not done a proper treatment of the stellar model atmosphere. Our models include lithium molecular formation, and predict that strong lithium lines remain at these temperatures.

6. Conclusions

In general we find that the "cleared-dust" model profiles fit the observed Cs I and Rb I resonance lines reasonably well. We further find that, in a given object, the effective temperatures derived independently from Cs I and Rb I agree to within ± 150K, with the Rb I fit consistently giving the higher temperature. We think this is due to the JOLA modeling of overlying molecular opacities at Rb I , and to what extent they overlap the atomic line. We find that the Cs I and Rb I analyses independently imply the same ordering of objects by effective temperature. The temperature scale derived from these lines may be a little hotter (100K) than that which seems to be coming out of consideration of low dispersion spectral energy distributions. There is no strong reason to prefer either scale at the moment but this one is better defined.

The treatment of dust is problematic. Although it must be true that there is rather little dust opacity in the far red (or we would not observe such strong atomic lines), it is not clear that our assumption of *no* opacity is valid. We must also reconcile the results in the far red with those in the near infrared, which apparently require more dust opacity. We suggest that the dust has largely settled out of the portion of the atmosphere sampled by the alkali resonance lines, but is present in

On the whole, we find good agreement between the models and the data with log[g]=5.0 and [M/H]=0.0. In the cases where the models do not reproduce the resonance lines very well, various effects may be responsible - collisional broadening effects due to surface gravity and/or metallicity variations, imperfectly modeled molecular opacity overlapping the line, or a low S/N ratio in the data. Our results further indicate that there may exist a degeneracy between the effects of T_{eff} and surface gravity in Cs I and Rb I , and that the two effects may be more easily sorted out by examining molecular bands.

We find that the molecular lines are not modeled as well as the resonance lines are, and that the fit to the molecular lines generally worsens as one moves lower in effective temperature. Both effects are expected, given the comparative paucity of well-determined parameters for many of the observed molecules. Obviously, given the sensitivity of the molecular lines to rotational velocity (and gravity and metallicity), it is desirable to improve our modeling of these lines. These affect the analysis of the objects at both high and low spectral dispersions (and in both the optical and near-IR).

One clear and fairly model independent result from our analysis is that the average rotation velocity of very low mass stars gets higher and higher as one moves down through the bottom of the main sequence. It is clear that as hydrogen burning begins to turn off near the substellar boundary, the magnetic braking which affects all higher mass convective stars is also weakening. Our sample is entirely from the field, and some objects are several hundred Myr old (although there is certainly an observational bias against finding very old objects, particularly if they are brown dwarfs). It appears that there is relatively little angular momentum evolution among these objects, and that they are typically born with relatively rapid rotation. Their lack of magnetic activity is seen directly (through a lack of Hα emission), as well as indirectly in their rapid rotation. The effort to understand these very low mass objects has just begun.

The temperature scale we find has led Martín et al. 1999b to propose a subclass designation scheme for the L spectral class slightly modified from that proposed by Kirkpatrick et al. 1999a. The new scheme begins with objects having about the same spectral appearance, but only extends to L6 (instead of L8) for the coolest current objects. Most objects end up with the same subclass designation as Kirkpatrick et al. 1999a. The L0 objects are at about 2200K, and each subclass is 100K cooler. The primary disagreement is on the subclass of the coolest objects. Because of the work here, Martín et al. 1999b classify them as L6, whereas Kirkpatrick et al. 1999a classified them as L8, believing them to be substantially cooler. Of course, this leads to a different mapping of spectral features onto subclasses, since both papers are attempting to define this mapping. Our hotter temperature leaves room for further spectral behavior (and spectral subclasses) between these L6 objects and the methane dwarfs (which should be cooler than 1400K). The coolest L stars (which will all be substellar) may well show some methane in some bands. The final determination of L star classifications should occur when the full range of temperatures down to objects like Gl 229B has been studied.

Acknowledgments: This research is based on data collected at the W. M. Keck Observatory, which is operated jointly by the University of California and California Institute of Technology. GB and SM acknowledge the support of NSF through grant AST96-18439. SM would like to thank GB and Don McCarthy (Steward Observatory) for invaluable mentorship. EM acknowledges support from the Fullbright-DGES program of the Spanish ministry of Education. AH's work is supported by the CNRS, a NASA LTSA NAG5-3435 and a NASA EPSCoR grant to Wichita State University. Some of the calculations presented in this paper were performed on the IBM SP2 of the CNUSC in Montpellier, and at the Cray T3E of the CEA in Grenoble. PHH's work was supported in part by NSF grant AST-9720704, NASA ATP grant NAG 5-3018 and LTSA grant NAG 5-3619 to the University of Georgia. Some of the calculations presented in this paper were performed on the IBM SP2 and the SGI Origin 2000 of the UGA UCNS and on the IBM SP of the San Diego Supercomputer Center (SDSC), with support from the National Science Foundation, and on the Cray T3E of the NERSC with support from the DoE. We thank all these institutions for a generous allocation of computer time.

A. Appendix

In §4.2, we noted that the calibrator used to determine the rotational velocities of target objects need not be a non-rotator. We empirically find that a relatively fast rotator can still be used as calibrator to determine the rotational velocities of target objects, so long as the target objects are rotating substantially faster than the calibrator. Here, we explore this effect in more detail. In particular we seek to answer the following questions:

1) What does "substantially faster" mean? Given an object rotating at a certain known velocity, what is the slowest rotating target for which this object can be used as a calibrator?

2) What are the errors we make in rotational velocity determination by using a relatively fast rotator as calibrator?

We review the method by which we determine the rotational velocity of a target object, using a (rotating) calibrator. Suppose the calibrator has a rotational velocity of v sin$i$ =$v1$, and the target has a rotational velocity of v sin$i$ =$v2$. We first find the correlation function, $\mathcal{C}_{ct}(\lambda)$, between the calibrator and the target. Next, we numerically rotationally broaden the spectrum of the (already rotating) calibrator by convolving the calibrator spectrum with rotational profiles corresponding to various velocities. Finally we correlate the spectrum of the original rotating calibrator with the artificially broadened ones; a given correlation function obtained is represented by $\mathcal{C}_{cv}(\lambda)$.

We assign a rotational velocity to the target by comparing $\mathcal{C}_{cv}(\lambda)$ and $\mathcal{C}_{ct}(\lambda)$. If $\mathcal{C}_{cv}(\lambda)$ = $\mathcal{C}_{ct}(\lambda)$ in the wavelength range considered then we assign to the target object the velocity v corresponding to the artificially broadened calibrator spectrum. For simplicity suppose that the calibrator spectrum alone, without the effects of *any* rotation, is only a δ-function. It is clear that, if the foregoing analysis is to yield approximately the correct value $v2$ for the rotational velocity of the target, then we must have:

$$[r(\Delta\lambda, v1) * r(\Delta\lambda, v2)] \simeq r(\Delta\lambda, v2) \tag{1}$$

where, $r(\Delta\lambda, v1)$ is the rotation profile corresponding to a rotation velocity of $v1$ and $r(\Delta\lambda, v2)$ is the rotation profile corresponding to a rotation velocity of $v2$. The form of the rotation profile for any v can be found in Gray 1992; it is roughly a semi-ellipse with a width that is directly proportional to v.

Eq.(1) states the condition which must be satisfied if a calibrator with $v1$ is to be used to correctly determine a target rotational velocity $v2$. When will this condition be true? Obviously, it will be precisely true if the calibrator is a non-rotator, i.e., if $v1 = 0$ (and thus $r(\Delta\lambda, v1)$ is a δ-function); this is why a non-rotating calibrator is ideal. However, if $v1 >$

0, then an analytical answer to this question is hard to find because, given the functional form of the rotation profile, the convolution represented on the left-hand side of eq.(1) results in a very complicated function, both in real and Fourier space. However, we can form a qualitative picture of when eq.(1) will be generally satisfied. We have noted that the width of the rotation profile is directly proportional to the velocity v. Hence, if the rotational velocity of the target is much larger than that of the calibrator, i.e., if $v2 \gg v1$, then $r(\Delta\lambda, v2)$ will be much wider than $r(\Delta\lambda, v1)$. In that case, $r(\Delta\lambda, v2)$ will dominate the convolution on the left-hand side of eq.(1); i.e., $[r(\Delta\lambda, v1) * r(\Delta\lambda, v2)] \rightarrow r(\Delta\lambda, v2)$ if $v2 \gg v1$, and eq.(1) is satisfied. This qualitatively supports our claim that a relatively fast rotator can be used as calibrator as long as the target rotates "substantially faster" than the calibrator.

We now empirically determine the lowest target $v \sin i$ which can be correctly deduced using a calibrator of given $v \sin i$. First, we simulate objects rotating at various velocities by rotationally broadening our observed spectrum of Gl 406. Then, $\mathcal{C}_{ct}(\lambda)$ and $\mathcal{C}_{cv}(\lambda)$ are evaluated by cross-correlating spectra artificially broadened by various rotational velocities, in the spectral range ~8630 - 8753A . For a given calibrator velocity $v1$ and target velocity $v2$, we then compare $\mathcal{C}_{cv}(\lambda)$ (evaluated at $v = v2$) with $\mathcal{C}_{ct}(\lambda)$. If $\mathcal{C}_{cv}(\lambda)$ and $\mathcal{C}_{ct}(\lambda)$ are indistinguishable, we conclude that a calibrator rotating at $v1$ can be used to identify a target rotating at $v2$. For a given calibrator velocity $v1$, the minimum $v2$ for which $\mathcal{C}_{ct}(\lambda)$ and $\mathcal{C}_{cv}(\lambda)$ are indistinguishable is the minimum target velocity that can be correctly deduced using that calibrator.

To compare $\mathcal{C}_{ct}(\lambda)$ and $\mathcal{C}_{cv}(\lambda)$, we fit a Gaussian profile to them and compare the Gaussian widths (Gaussians fit the correlation functions well). This is done to obtain a single objective measure of the similarity between $\mathcal{C}_{ct}(\lambda)$ and $\mathcal{C}_{cv}(\lambda)$. In particular, $\mathcal{C}_{ct}(\lambda)$ and $\mathcal{C}_{cv}(\lambda)$ are deemed to be sufficiently alike when the widths of their respective Gaussian fits differ by $\leq$ a certain percentage. What percentage should we use? Since our actual determination of rotational velocities were based on comparing $\mathcal{C}_{ct}(\lambda)$ and $\mathcal{C}_{cv}(\lambda)$ by eye, the chosen percentage should be one that results in $\mathcal{C}_{cv}(\lambda)$ and $\mathcal{C}_{ct}(\lambda)$ being indistinguishable to the eye. A single criterion cannot be applied at all velocities. For example, using target velocities up to 40 km s^{-1} with a calibrator velocity of 5 km s^{-1} , Gaussian widths within 10% are visually indistinguishable, whereas for calibrators above 10 km s^{-1} they must be within 5% of each other.

One important point must be made here about errors. The above analysis indicates that for a given calibrator velocity $v1$ and a high enough target velocity $v2$, $\mathcal{C}_{ct}(\lambda)$ will be indistinguishable from $\mathcal{C}_{cv}(\lambda)$ evaluated at $v{=}v2$, and thus the correct target velocity $v2$ will be deduced by comparing $\mathcal{C}_{ct}(\lambda)$ and $\mathcal{C}_{cv}(\lambda)$. However, it is possible that $\mathcal{C}_{cv}(\lambda)$

evaluated at v=$v2 \pm \delta v$ will *also* be indistinguishable from $\mathcal{C}_{ct}(\lambda)$, leading to a range in our determination of $v2$. We have checked our correlation functions for this effect, and find that for target velocities up to 60 km s^{-1} , using calibrators with velocities 0-20 km s^{-1} leads to errors of $\lesssim \pm 7$ km s^{-1} , with the errors being lowest for "low calibrator velocity with low target velocity" cases, and highest for "high calibrator velocity with high target velocity" cases. These errors are noted in Table 2.

We find that the minimum target velocity for a calibrator with v sin$i$ = 10 km s^{-1} is $\sim$30 km s^{-1} , with an error of $\pm$1 km s^{-1} . That is, when we cross-correlate a calibrator with v sin$i$ =10 km s^{-1} with a target of *known* v sin$i$ =30 km s^{-1} , the v sin$i$ *derived* for the target is 30 $\pm$1 km s^{-1} . Thus we are justified in using 2MASSW 1439+1929 (v sin$i$ =10 km s^{-1}) as calibrator to deduce the rotational velocities of those cooler L-dwarfs which appear to rotate faster than 30 km s^{-1} (as estimated from profile-fitting). However, some of the cooler L-dwarfs appear, from profile-fitting, to have a v sin$i$ < 30 km s^{-1} . How can we justify using 10 km s^{-1} calibrator to derive precisely the rotational velocities of these objects?

Returning to eq.(1), we see that if we use a calibrator rotating at a finite velocity (e.g., 10 km s^{-1}), then $r(\Delta\lambda, v1)$ has a finite width, so the convolution $[r(\Delta\lambda, v1) * r(\Delta\lambda, v)]$ for any given v will be *wider* than if we had used a non-rotating calibrator (for which $r(\Delta\lambda, v1)$ is a δ-function). [8] Thus, eq.(1) will appear to be satisfied at a v which is *less than* $v2$. For example, suppose we have a 10 km s^{-1} calibrator and a 10 km s^{-1} target. Then cross-correlating the calibrator and target will yield a convolution function that is identical to that resulting from cross-correlating the calibrator with itself *without any artificial broadening.* Thus, if we did not correct for the fact that the calibrator is already rotating at 10 km s^{-1} , we would infer that the target has v sin$i$ = 0 km s^{-1} , which is incorrect.

In general, we qualitatively expect that using a 10 km s^{-1} calibrator will lead us to infer target velocities *systematically lower* than the actual target velocity values. This effect should diminish as we go to larger and larger target velocities, until it becomes vanishingly small for target velocities $\geq$ the minimum correctly diagnosable target velocity (by definition of the latter). Inversely, this effect should grow as the target velocity becomes less than the minimum correctly diagnosable velocity and approaches the calibrator velocity more and more closely. Furthermore, once the target velocity becomes *less* than the calibrator velocity, eq.(1) becomes dominated by the rotation profile of the *calibrator*, and

---

[8] The convolution function will also be a slightly different shape from that for a non-rotating calibrator, since the convolution of two rotation profiles is *not* another rotation profile, but this is a second-order effect that is unimportant for this qualitative discussion.

no meaningful rotational velocity is derivable for the target. All these predictions are borne out by our actual correlation functions. The important point about this effect is that it is systematic, so that as long as the true target velocity is greater than the calibrator velocity, it can be precisely determined by applying an additive correction factor to the velocity derived through cross-correlation. If we consider again, for example, the case discussed above in which both the calibrator and target are rotating at 10 km s^{-1} , the true target velocity (10 km s^{-1}) can be inferred by adding a correction factor (+10 km s^{-1}) to the velocity derived through cross-correlation (0 km s^{-1}). This is possible because, for a given calibrator velocity, there is a one-to-one mapping between a velocity derived through cross-correlation and the corresponding correction factor (resulting from the fact that the width of the rotation profile grows monotonically with increasing velocity).

Thus, since all the cool L-dwarfs with v sin$i$ < 30 km s^{-1} are nevertheless rotating faster than 10 km s^{-1} , it is possible to use G196-3B or 2MASSW 1439+1929 to determine their v sin$i$ accurately, by applying the appropriate correction factors. For a 10 km s^{-1} calibrator, we empirically determine these factors by cross-correlating spectra artificially broadened by various amounts. The factors turn out to be relatively small, and rapidly become smaller as the target velocity increases, as expected. For a derived target velocity of 10 km s^{-1} , for example, the true target velocity is 15 km s^{-1} , while for a derived target velocity of 24 km s^{-1} , the true velocity is 25 km s^{-1} . For the objects in our sample, the correction factors are all $\lesssim$ 2 km s^{-1} .

REFERENCES

Allard, F., Hauschildt, P.H., Baraffe, I., Chabrier, G., 1996, ApJLetters, 465, L123

Allard, F., Hauschildt, P., Alexander, D.R., Starrfield, S., 1997, ARA&A, 35, 137

Allard, F., 1998, Astronomical Society of the Pacific Conference Series, 134, 370, ed. Rebolo, R., Martín, E.L., Zapatero Osorio, M.R.

Baraffe, I., Chabrier, G., Allard, F., Hauschildt, P.H., 1998, A&A, 337, 403

Basri, G., Marcy, G.W., 1995, AJ, 109, 762

Basri, G., Marcy, G.W., Oppenheimer, B., Kulkarni, S.R., Nakajima, T., 1996, in Cool Stars, Stellar Systems & the Sun, 9th Cambridge Workshop, ASP Conference Series, 109, ed. Pallavicini, R. & Dupree, A.K.

Becklin, E.E. & Zuckerman, B., 1988, Nature, 336, 656

Burrows, A., Marley, M., Hubbard, W.B., Lunine, J.I., Guillot, T., Saumon, D., Freedman, R., Sudarsky, D., Sharp, C., 1997, ApJ, 491, 856

Burrows, A., Marley, M., Sharp, C.M., 1999, ApJ, submitted

Delfosse, X., Forveille, T., Perrier, C., Mayor, M., 1998, A&A, 331, 581

Delfosse, X., Tinney, C.G., Forveille, T., Epchtein, N., Borsenberger, J., Foque, P., Kimeswenger, S., Tiphene, D., 1999, A&AS, 135, 41

DeJager, C. & Nieuwenhuijzen, H., 1987, A&A, 177, 217

Golimowski, D.A., Burrows, C.J., Kulkarni, S.R., Oppenheimer, B.R., Brukardt, R.A., 1998, AJ, 115, 2579

Goldman, B., Delfosse, X., Forveille, T., Afonso, C. et al., 1999, A&A, in press

Gray, D.F. 1992, *The Observation and Analysis of Stellar Photospheres, 2nd Ed.*, New York:Cambridge Univ. Press

Griffith, C.A., Yelle, R.V., Marley, M.S., 1998, Science, 282, 2063

Hauschildt, P.H., Allard, F., Baron, E. 1999, ApJ, 512, 377

Jones, H.R.A., Tsuji, T., 1997, ApJ, 408, 39

Jones, H.R.A., Longmore, A.J., Jameson, R.F., Mountain, C.M., 1994, MNRAS, 267, 413

Kirkpatrick, J.D., Henry, T.J., Irwin, M.J., 1997, AJ, 113, 1421

Kirkpatrick, J.D. et al., 1999a, ApJ, 519, 802

Kirkpatrick, J.D. et al., 1999b, ApJ, 519, 834

Leggett, S.K., Allard, F., Hauschildt, P.H., 1998, ApJ, 509, 836

Martín, E.L., Basri, G., Delfosse, X., Forveille, T., 1997, A&A, 327, L29

Martín, E.L., Brandner, W., Basri, G., 1999a, Science, 238, 1718

Martín, E.L., Delfosse, X., Basri, G., Goldman, B., Forveille, T., Zapatero Osorio, M.R. 1999b, AJ(accepted - Nov. 1999)

Oppenheimer, B.R., Kulkarni, S.R., Matthews, K., Van Kerwijk, M.H., 1998, ApJ, 502, 932

Rebolo, R., Zapatero Osorio, M.R., Madruga, S., Bejar, V.J.S., Arribas, S., Licandro, J., 1998, Science, 282, 1309

Ruiz, M.T., Leggett, S.K., Allard, F., 1997, ApJ, 491, L110

Schweitzer, A., Hauschildt, P.H., Allard, F., Basri, G., 1996, MNRAS, 283, 821

Sharp, C.M., Huebner, W.F., 1990, ApJS, 72, 417

Tinney, C.G., Reid, I.N., 1998, MNRAS, 301, 1031

Tinney, C.G., 1998, MNRAS, 296, L42

Tinney, C.G., Delfosse, X., Forveille, T., Allard, F., 1998, A&A, 338, 1066

Tokunaga, A.T., Kobayashi, N., 1999, AJ, 117, 1010

Tsuji, T., Ohnaka, K., Aoki, W., Nakajima, T., 1996b, A&A, 308, L29

Tsuji, T., Ohnaka, K., Aoki, W., 1996a, A&A, 305, L1

Vogt, S. et al., 1994, in Instrumentation in Astronomy III, Proc. SPIE, 2198, 362, ed. Crawford, D.L., Craine, E.R.

This preprint was prepared with the AAS LaTeX macros v4.0.

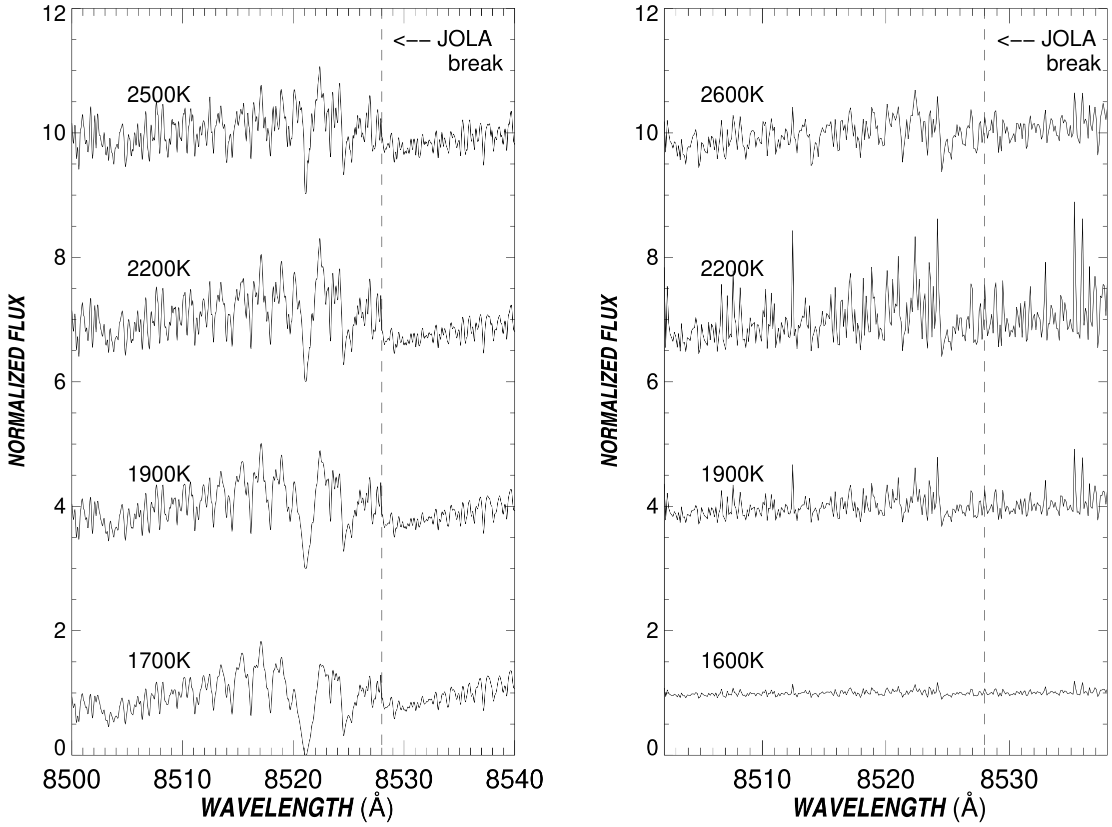

Fig. 1.— *Left panel*: Standard (no-dust) models for Cs I , with the JOLA break indicated. Molecular opacity allows only the core of the resonance line to be seen. *Right panel*: Dusty models for Cs I . Veiling due to dust makes the resonance line appear very weak. The molecular features have changed due to depletion of elements into the dust phase. Each model is offset upwards by three from the lower model. In these figures and all following ones, log[g]=5.0 and [M/H]=0.0

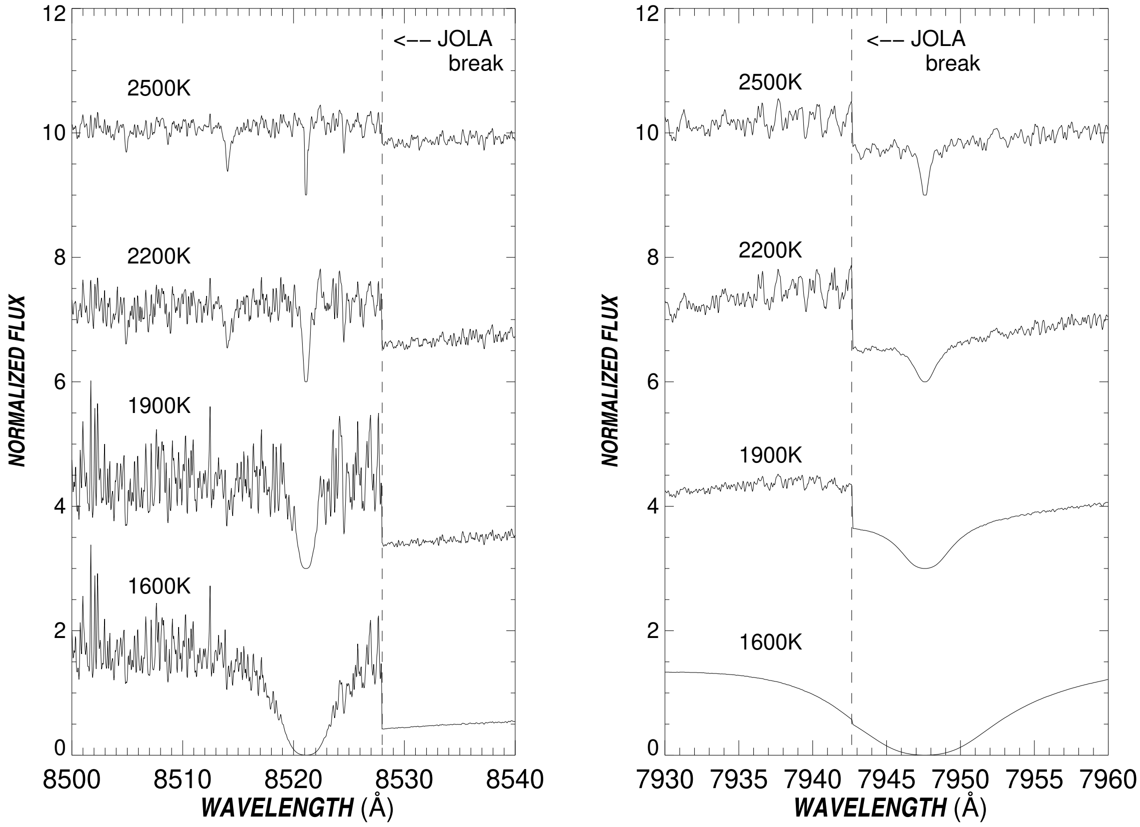

Fig. 2.— *Left panel*: Cleared-dust models for Cs I . *Right panel*: Cleared-dust models for Rb I . In both cases, the absence of significant molecular and dust opacities allows the molecular lines and resonance line to be much stronger than in the standard and dusty models. The JOLA break in the cleared-dust models is also much stronger than in the standard and dusty models.

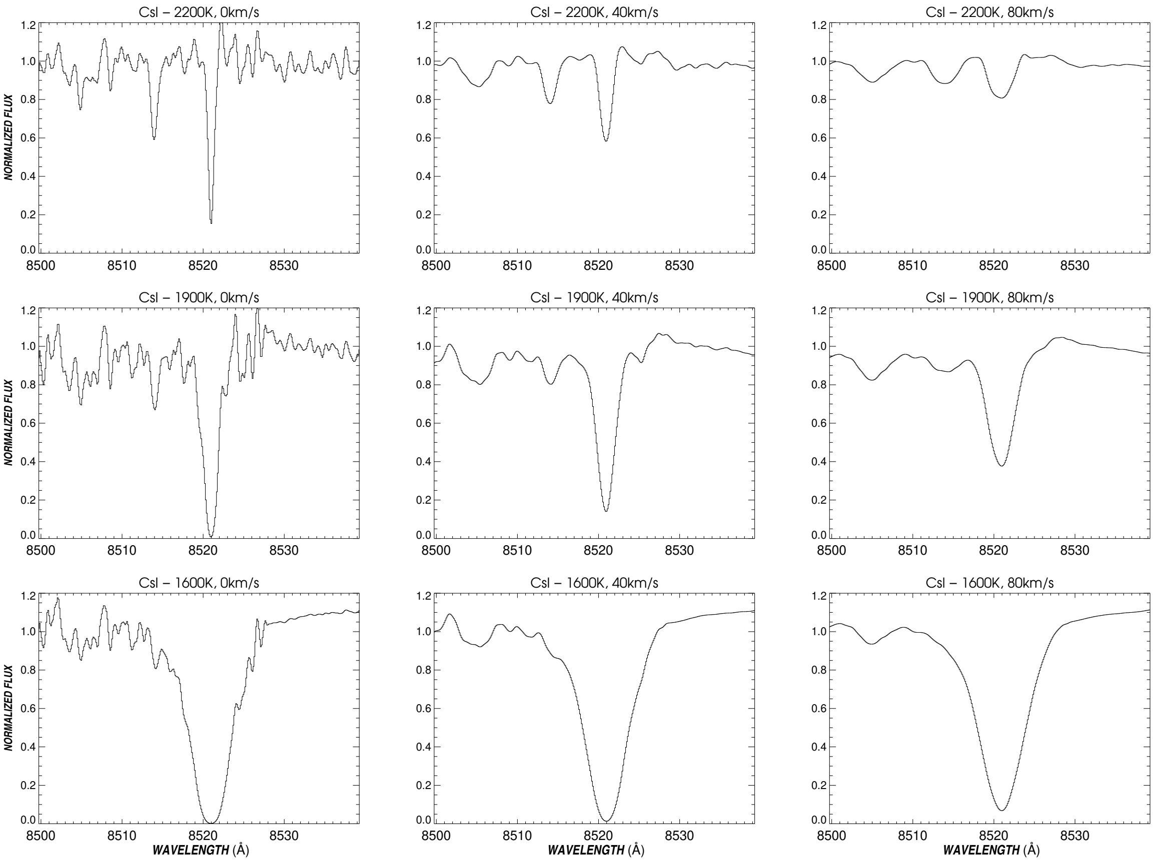

Fig. 3.— Effect of T_{eff} and v sin$i$ on line profile, for cleared-dust models. Temperatures of 1600, 1900 and 2200K are shown from bottom to top; v sin$i$ of 0, 40 and 80 km s^{-1} are shown from left to right. Decreasing T_{eff} causes the Cs I line to become stronger, increasing in both depth and width. Increasing v sin$i$ also increases the width of the line, but decreases its depth, thus making it possible to distinguish between changes in T_{eff} and changes in v sin$i$. At $T_{eff} \lesssim$ than 1600K (last row), collisional broadening of the resonance line overwhelms the rotational broadening, and it is no longer possible to infer v sin$i$ from the resonance line profile. The sharpness of molecular lines, on the other hand, is relatively unaffected by T_{eff} , but highly influenced by v sin$i$; thus molecular lines can be used to infer v sin$i$ information even at low T_{eff} .

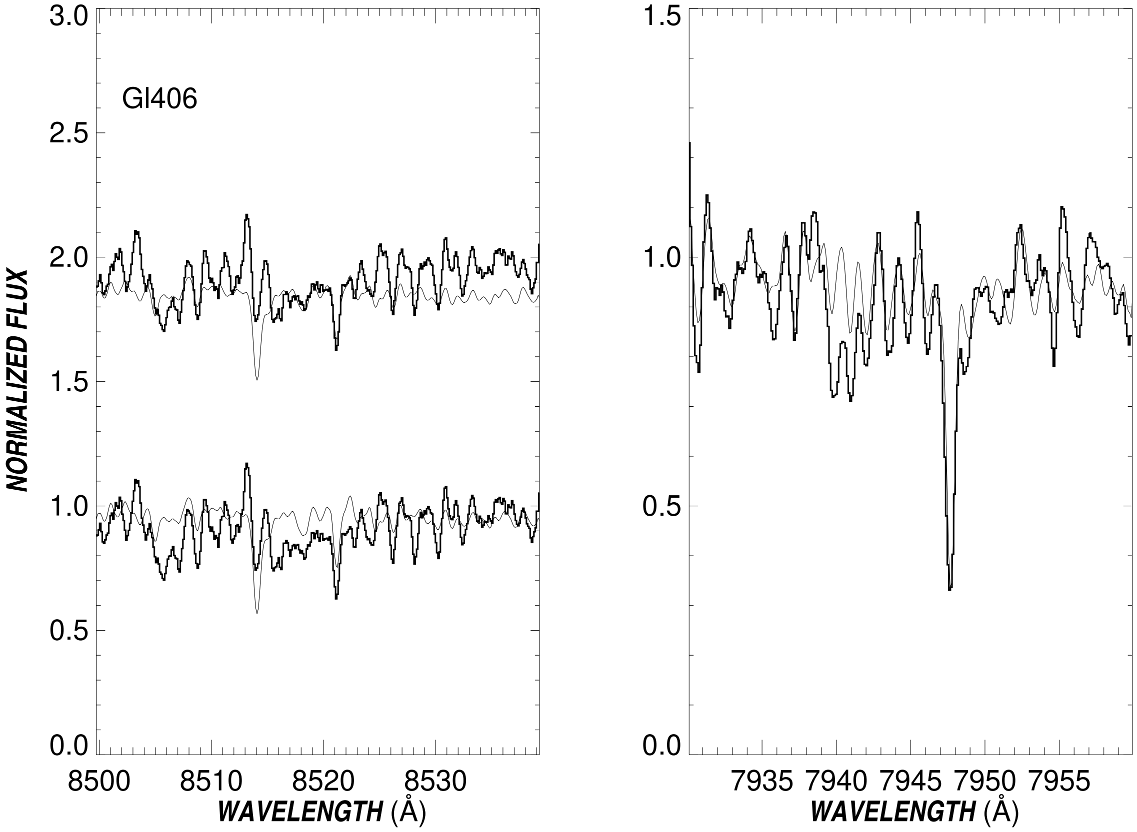

Fig. 4.— *Left panel*: Bottom - Gl 406 Cs I spectrum (thick solid histogram), with 2800K (thin solid line) cleared-dust model at 0 km s^{-1} . Top - Same, but with the model now renormalized to the spectral interval 8516-8524A , to give a better fit to the observed line. The observed spectrum and the model (after renormalization) are offset by 1 from the bottom panel. *Right panel*: Gl 406 Rb I spectrum (thick solid hist.), with 2700K cleared-dust model at 0 km s^{-1} (thin solid line).

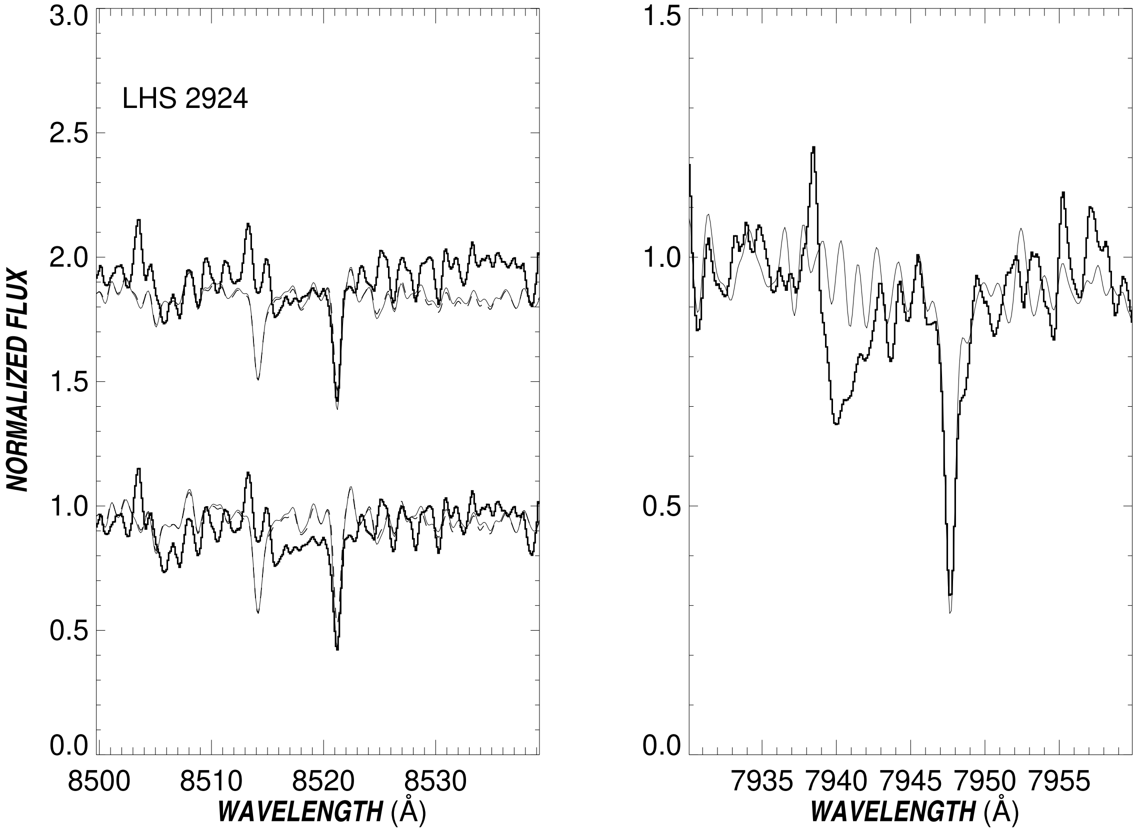

Fig. 5.— *Left panel*: LHS 2924 Cs I spectrum, with 2400K (thin solid line) and 2500K (thin dashed line) cleared-dust models at 10 km s^{-1} . *Right panel*: LHS 2924 Rb I spectrum, with 2600K cleared-dust model at 10 km s^{-1} .

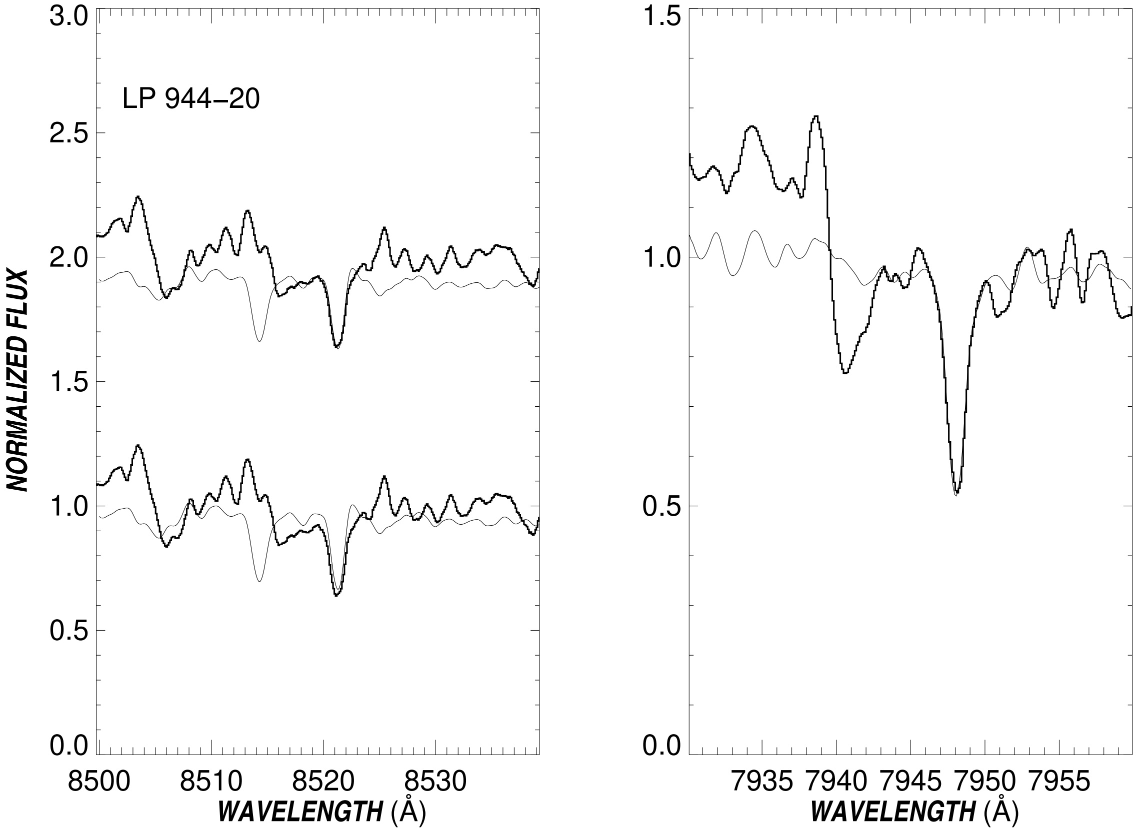

Fig. 6.— *Left panel*: LP 944-20 Cs I spectrum, with 2400K cleared-dust model at 30 km s^{-1} . *Right panel*: LP 944-20 Rb I spectrum, with 2600K cleared-dust model at 30 km s^{-1} .

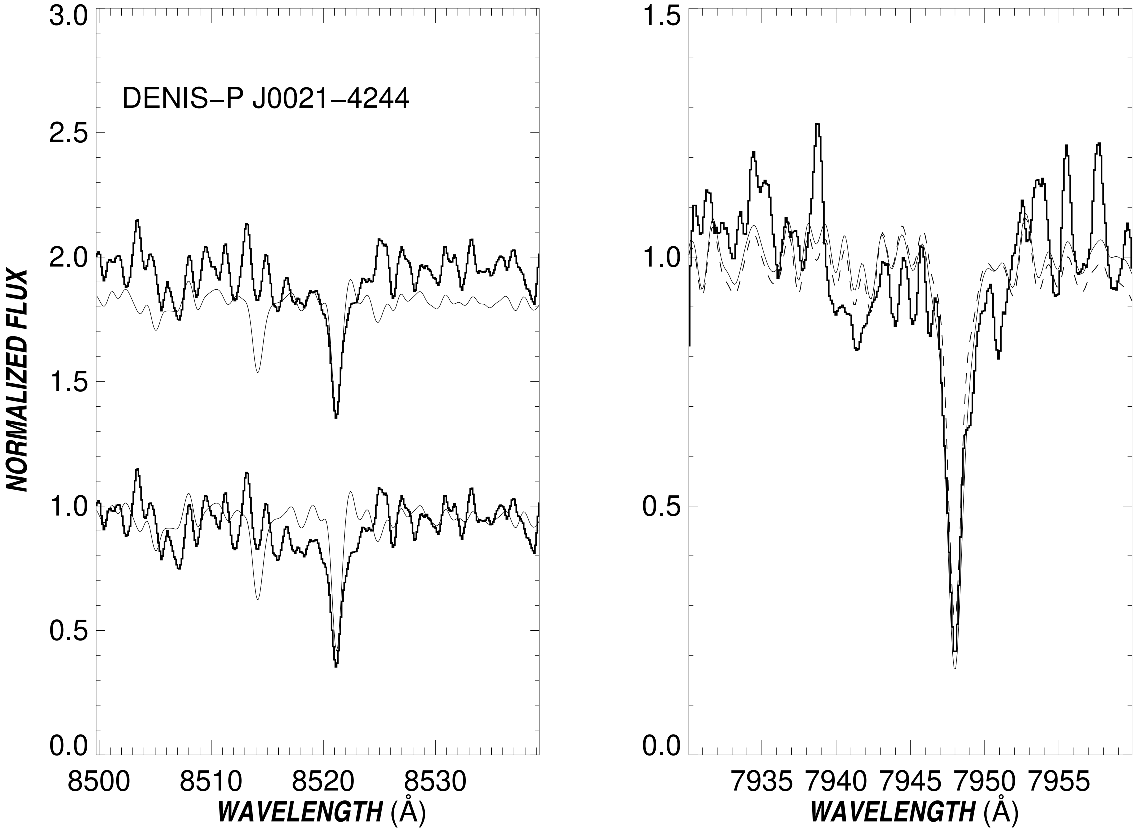

Fig. 7.— *Left panel*: DENIS-P J0021-4244 Cs I spectrum, with 2300K cleared-dust model at 17.5 km s^{-1} . *Right panel*: DENIS-P J0021-4244 Rb I spectrum, with 2400K (thin solid line) and 2500K (thin dashed line) cleared-dust models at 17.5 km s^{-1} .

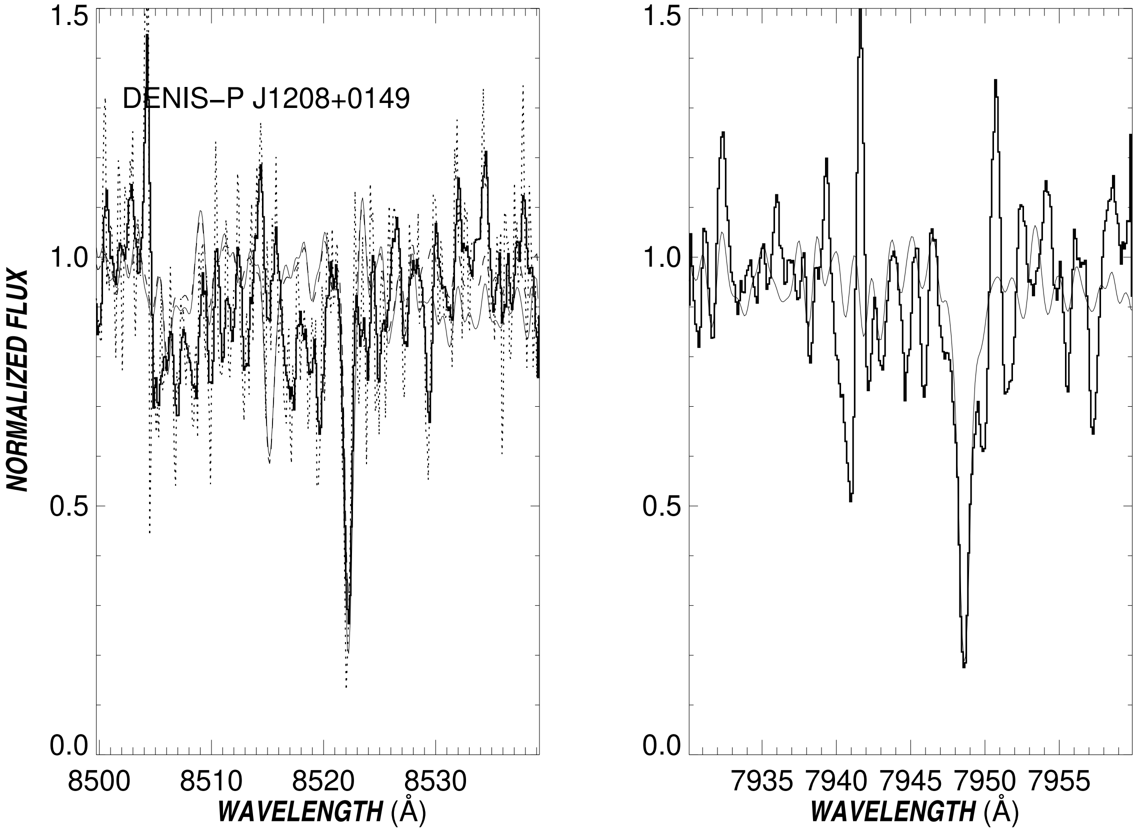

Fig. 8.— *Left panel*: DENIS-P J1208+0149 Cs I spectrum, with 2200K (thin solid line) and 2300K (thin dashed line) cleared-dust models at 10 km s^{-1} . Also shown is the unsmoothed data (dotted line) to show the unsmoothed intensity at the edges of the observed Cs I line, and the unsmoothed depth of the observed Cs I line core, both of which the models match well. *Right panel*: DENIS-P J1208+0149 Rb I spectrum, with 2500K cleared-dust model at 10 km s^{-1} .

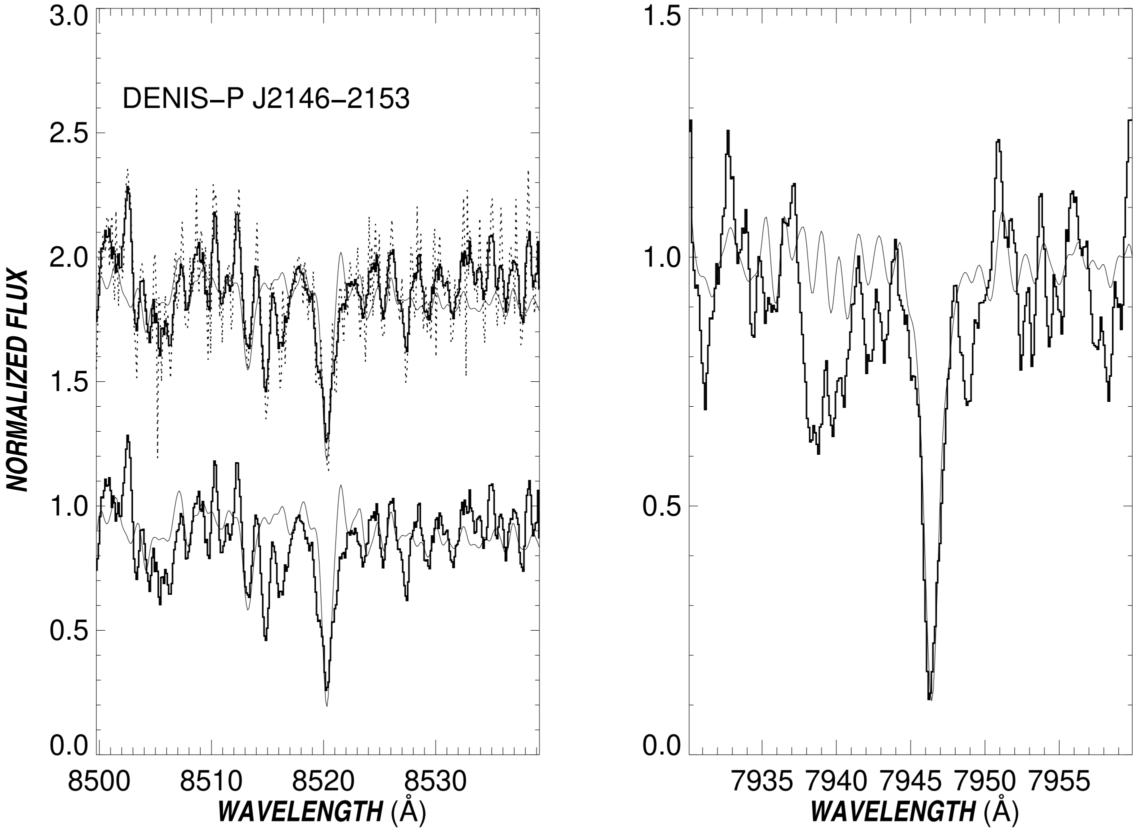

Fig. 9.— *Left panel*: DENIS-P J2146-2153 Cs I spectrum , with 2200K cleared-dust model at 10 km s^{-1} . The top panel also shows the unsmoothed data (dotted line) to show the unmodeled molecular lines within the Cs I line, and the unsmoothed depth of the Cs I line. *Right panel*: DENIS-P J2146-2153 Rb I spectrum, with 2400K cleared-dust model at 10 km s^{-1} .

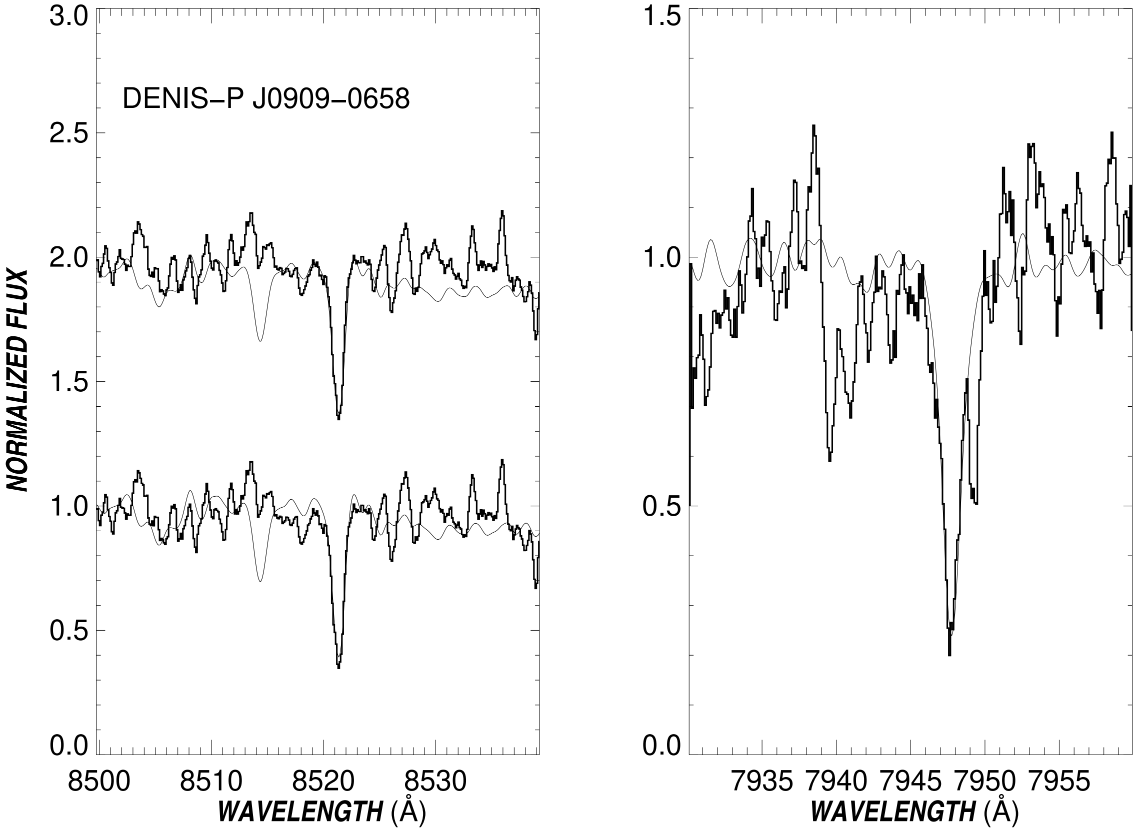

Fig. 10.— *Left panel*: DENIS-P J0909-0658 Cs I spectrum, with 2200K cleared-dust model at 25 km s^{-1} . *Right panel*: DENIS-P J0909-0658 Rb I spectrum, with 2400K cleared-dust models at 25 km s^{-1} .

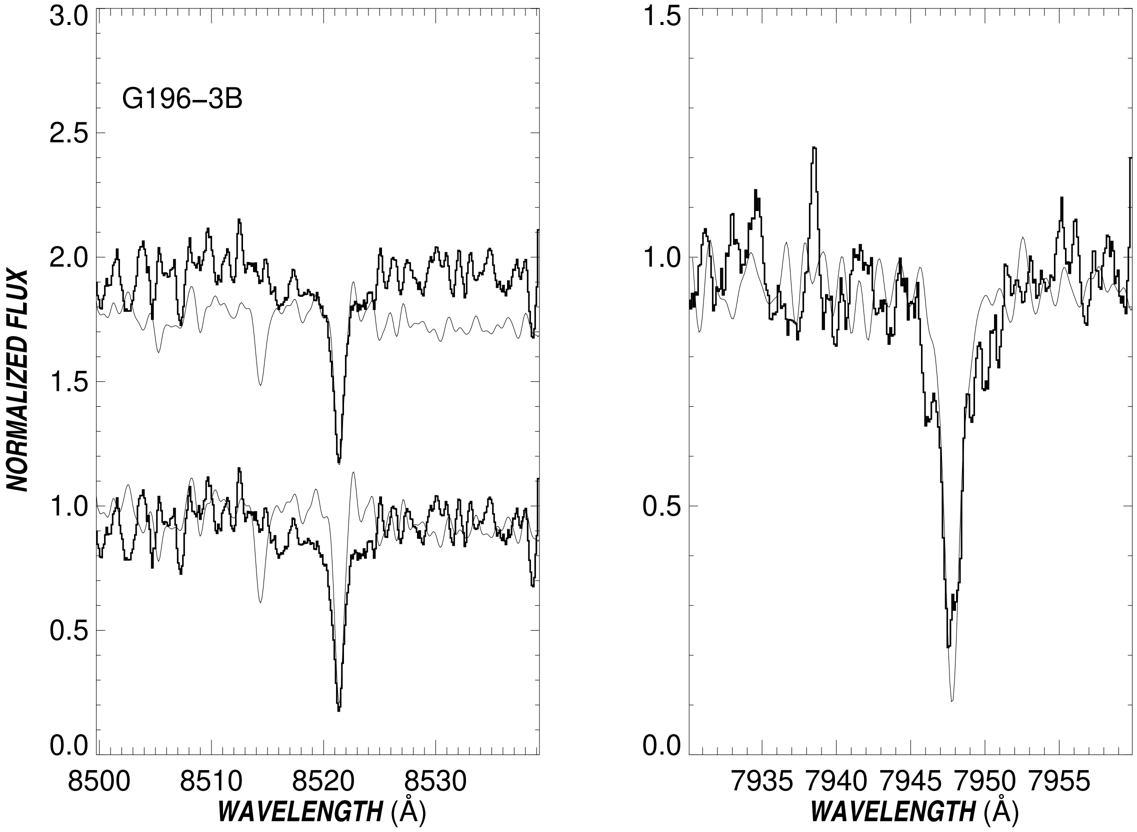

Fig. 11.— *Left panel*: G 196-3B Cs I spectrum , with 2200K cleared-dust model at 10 km s^{-1} . *Right panel*: G 196-3B Rb I spectrum, with 2400K cleared-dust model at 10 km s^{-1} .

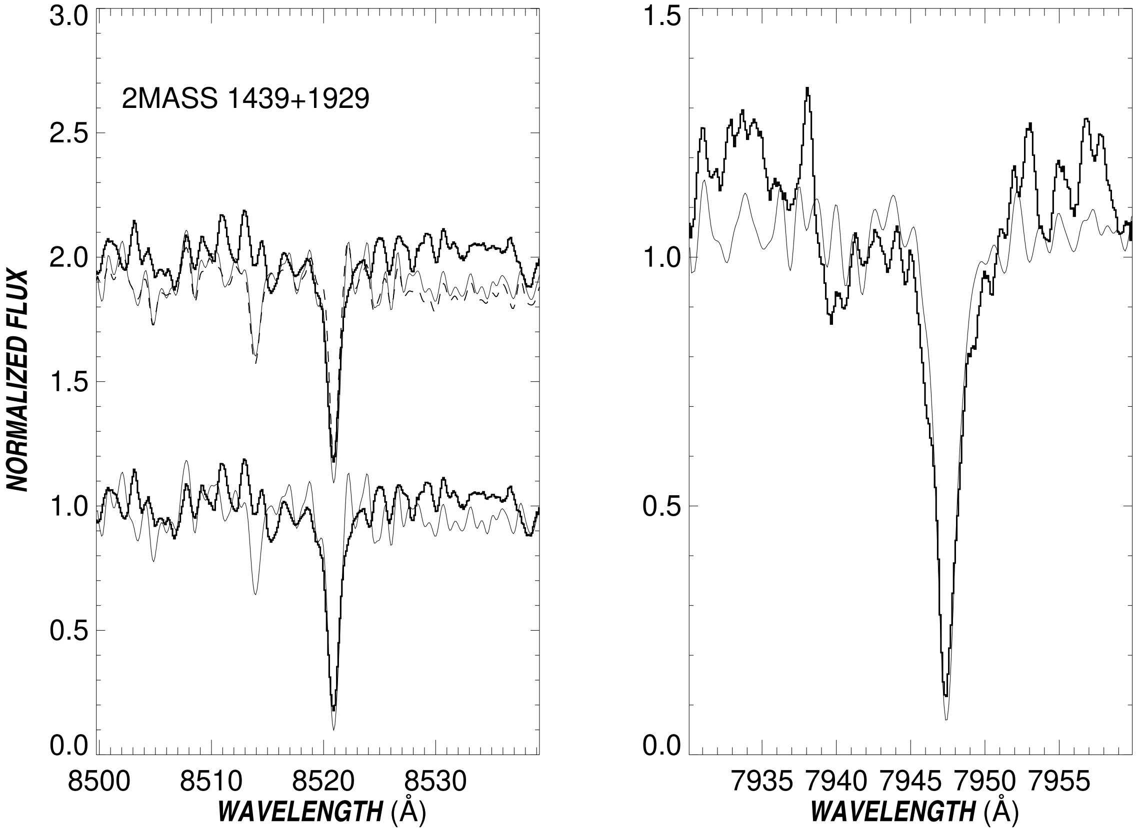

Fig. 12.— *Left panel*: 2MASSW 1439+1929 Cs I spectrum, with 2100K (thin solid line) and 2200K (thin dashed line) cleared-dust model at 10 km s^{-1} . *Right panel*: 2MASSW 1439+1929 Rb I spectrum, with 2300K cleared dust model at 10 km s^{-1} .

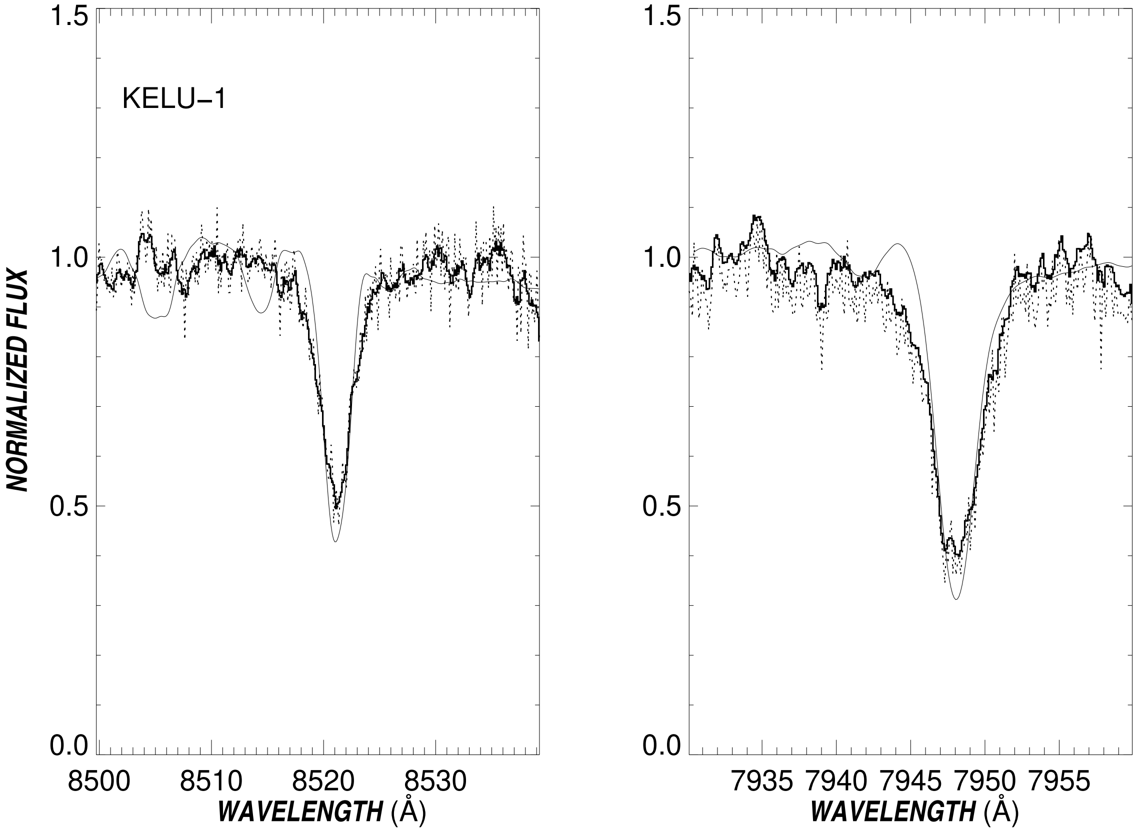

Fig. 13.— *Left panel*: Kelu-1 Cs I spectrum , with 2000K (thin solid line) cleared-dust model at 60 km s^{-1} . Also shown is the unsmoothed data (dotted line) to show the unmodeled molecular lines within the Cs I line, and the unsmoothed depth of the Cs I line. *Right panel*: Kelu-1 Rb I spectrum, with 2200K (thin solid line) cleared-dust model at 60 km s^{-1} . The unsmoothed data (dotted line) is again shown, for the same purpose. This object is the fastest rotator in our sample.

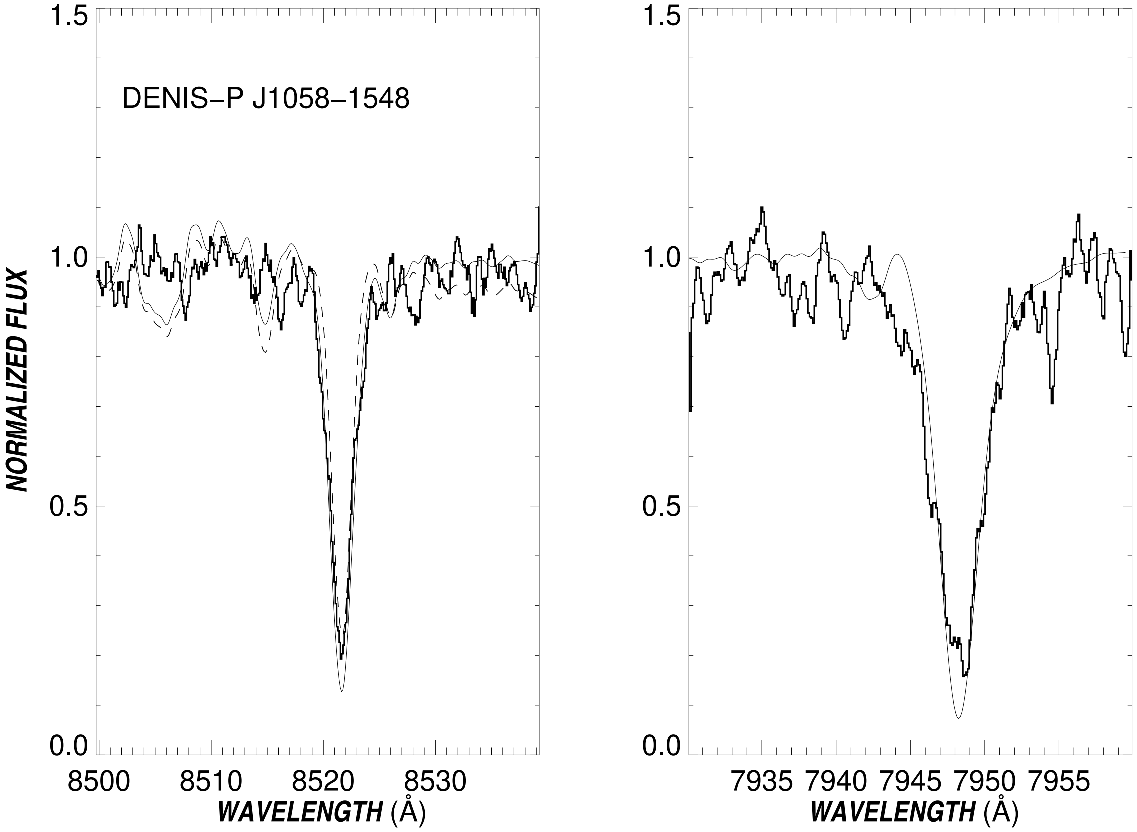

Fig. 14.— *Left panel*: DENIS-P J1058-1548 Cs I spectrum, with 1900K (thin solid line) and 2000K (thin dashed line) cleared-dust models at 37.5 km s^{-1} . *Right panel*: DENIS-P J1058-1548 Rb I spectrum, with 2000K cleared-dust model at 37.5 km s^{-1} .

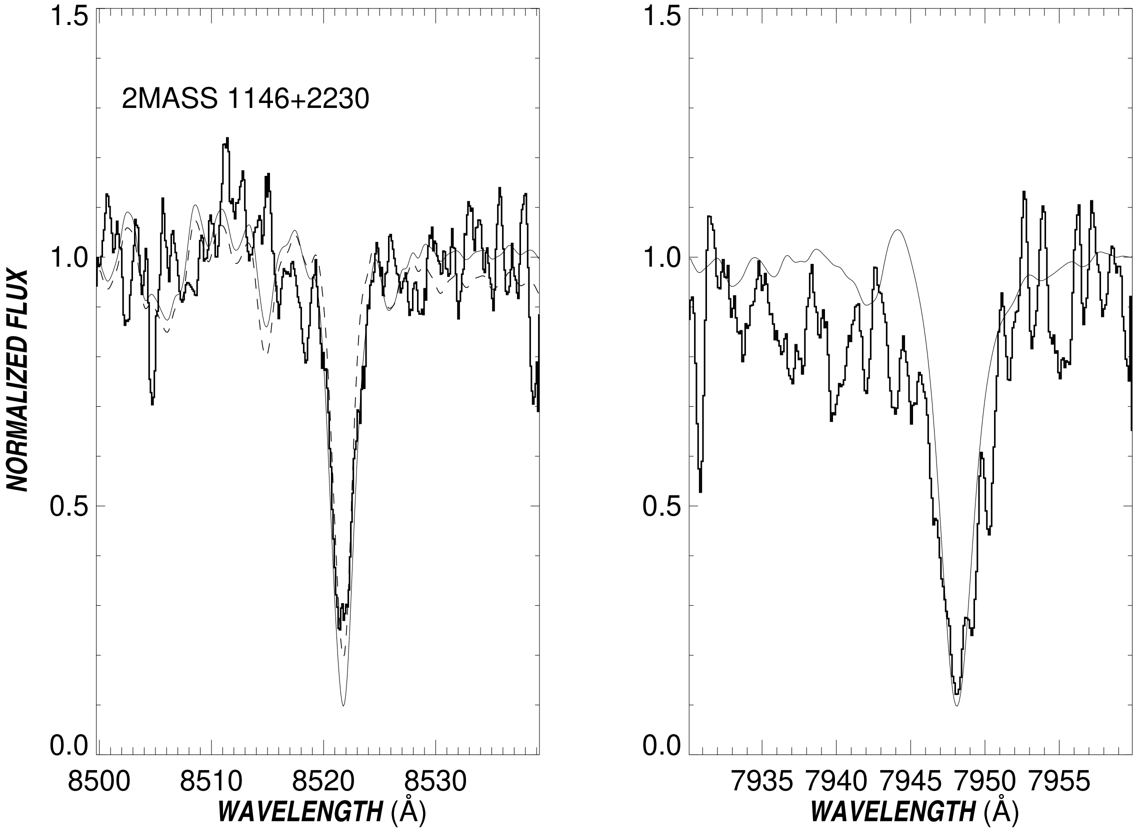

Fig. 15.— *Left panel*: 2MASSW 1146+2230 Cs I spectrum, with 1900K (thin solid line) and 2000K (thin dashed line) cleared-dust model at 32.5 km s^{-1} . *Right panel*: 2MASSW 1146+2230 Rb I spectrum, with 2100K cleared dust model at 32.5 km s^{-1} .

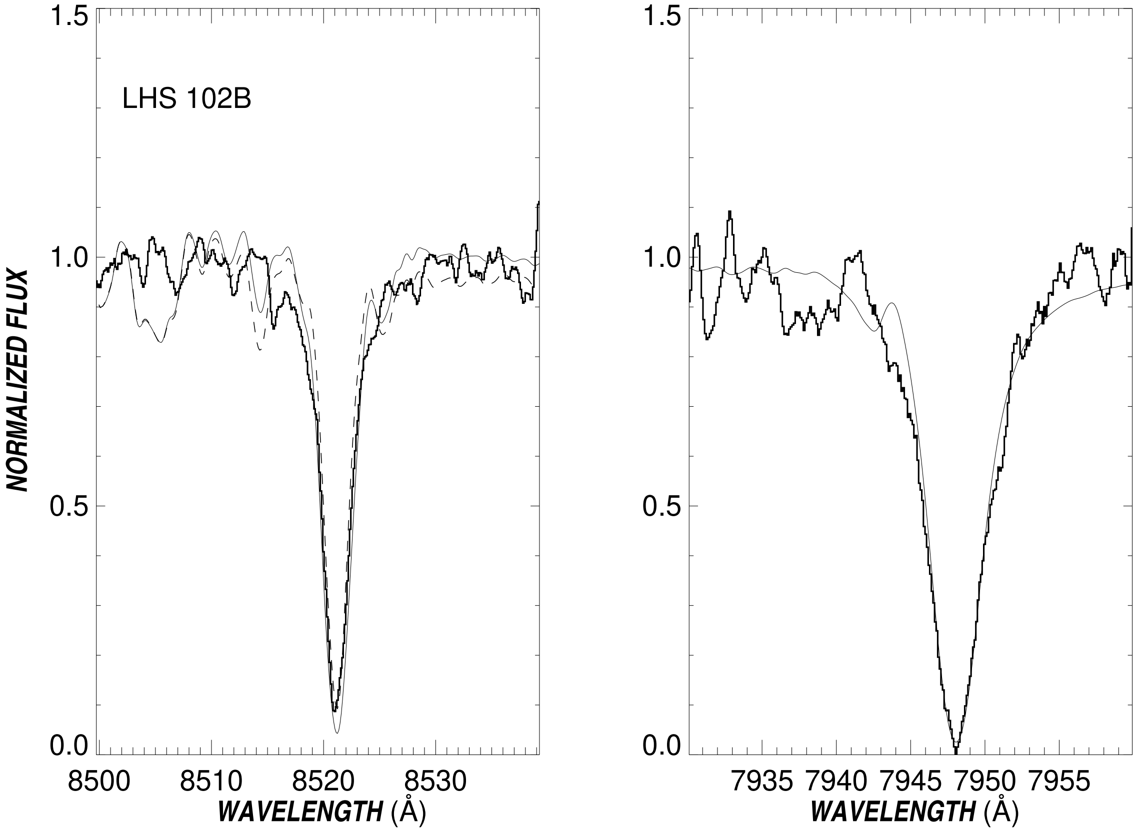

Fig. 16.— *Left panel*: LHS 102B Cs I spectrum with 1800K (thin solid line) and 1900K (thin dashed line) cleared-dust models at 32.5 km s^{-1} . *Right panel*: LHS 102B Rb I spectrum, with 1900K cleared-dust model at 32.5 km s^{-1} .

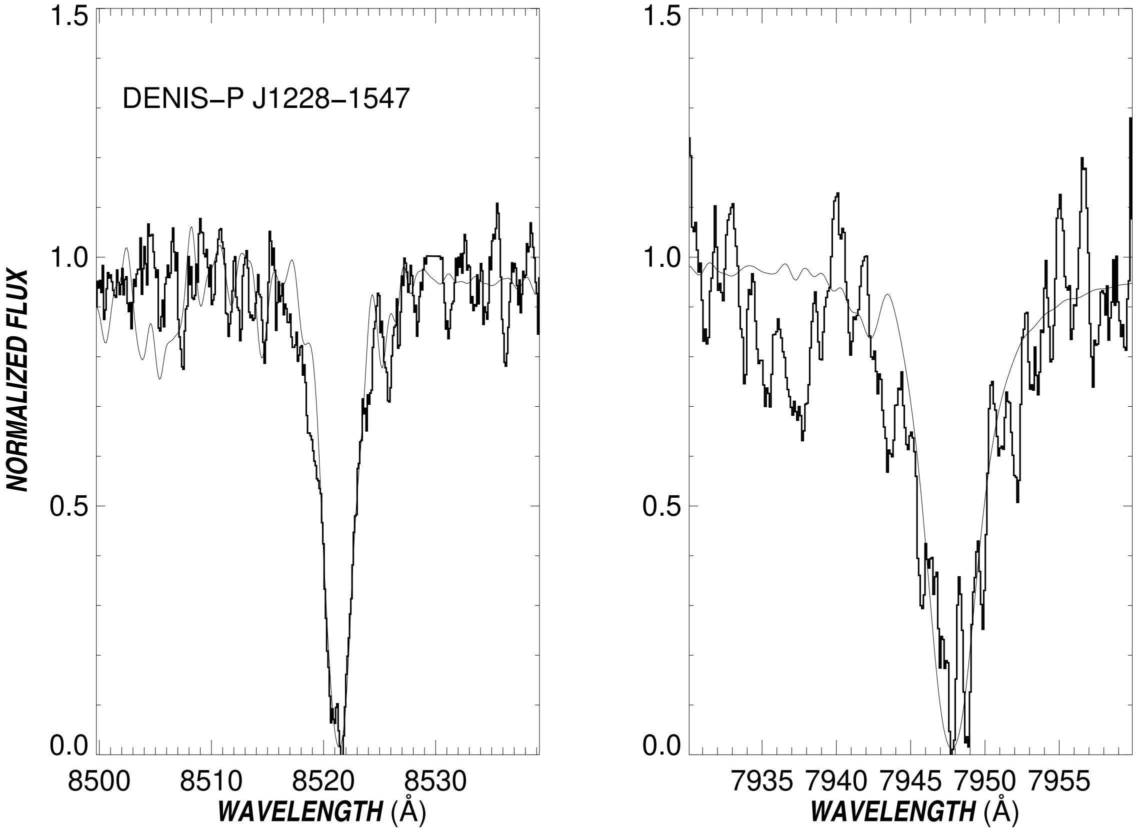

Fig. 17.— *Left panel*: DENIS-P J1228-1547 Cs I spectrum , with 1800K cleared-dust model at 22 km s^{-1} . *Right panel*: DENIS-P J1228-1547 Rb I spectrum, with 1900K cleared-dust models at 22 km s^{-1} . Both spectra appear noisy, and the Rb I fit is crude. This object is a binary, and it is possible that we are looking at a composite spectrum.

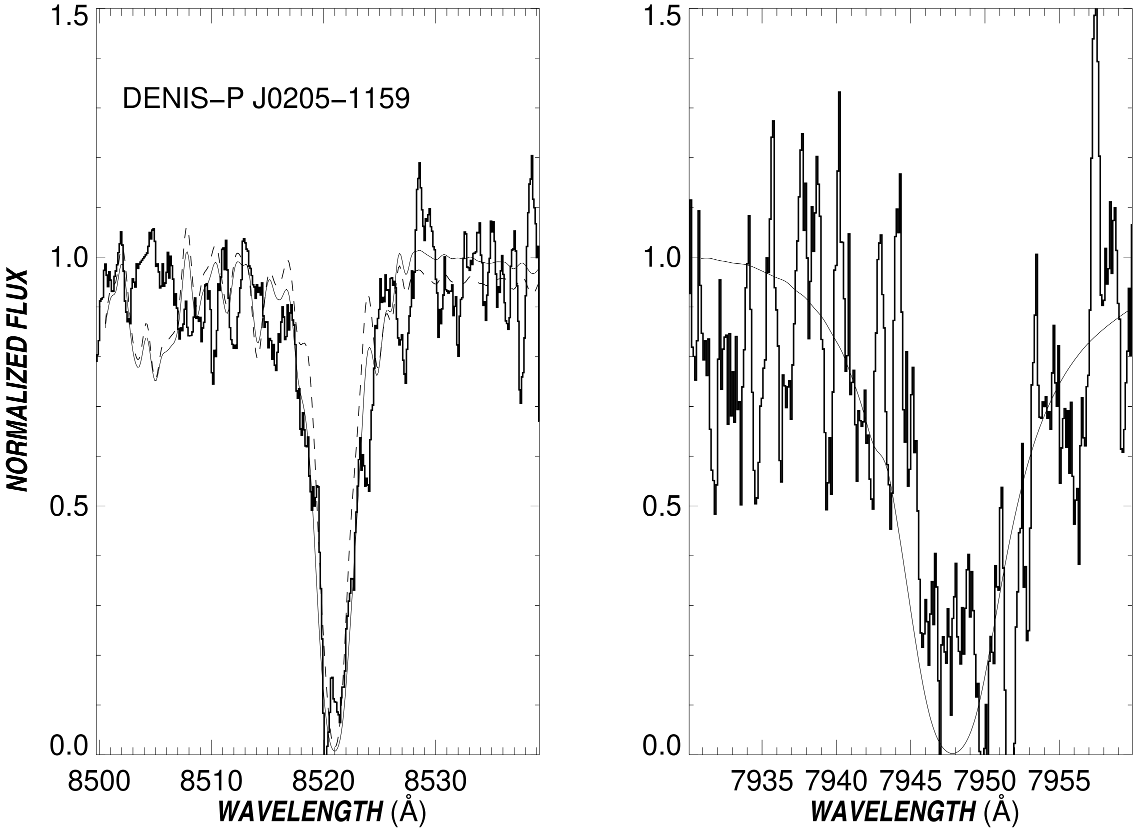

Fig. 18.— *Left panel*: DENIS-P J0205-1159 Cs I spectrum , with 1700K (thin solid line) and 1800K (thin dashed line) cleared-dust models at 22 km s^{-1} . *Right panel*: DENIS-P J0205-1159 Rb I spectrum, with 1700K cleared-dust model at 22 km s^{-1} . Due to the low S/N of the Rb I spectrum, no best fit was found; the model shown is for comparison only to the Cs I fit at the same T_{eff} and rotational velocity.

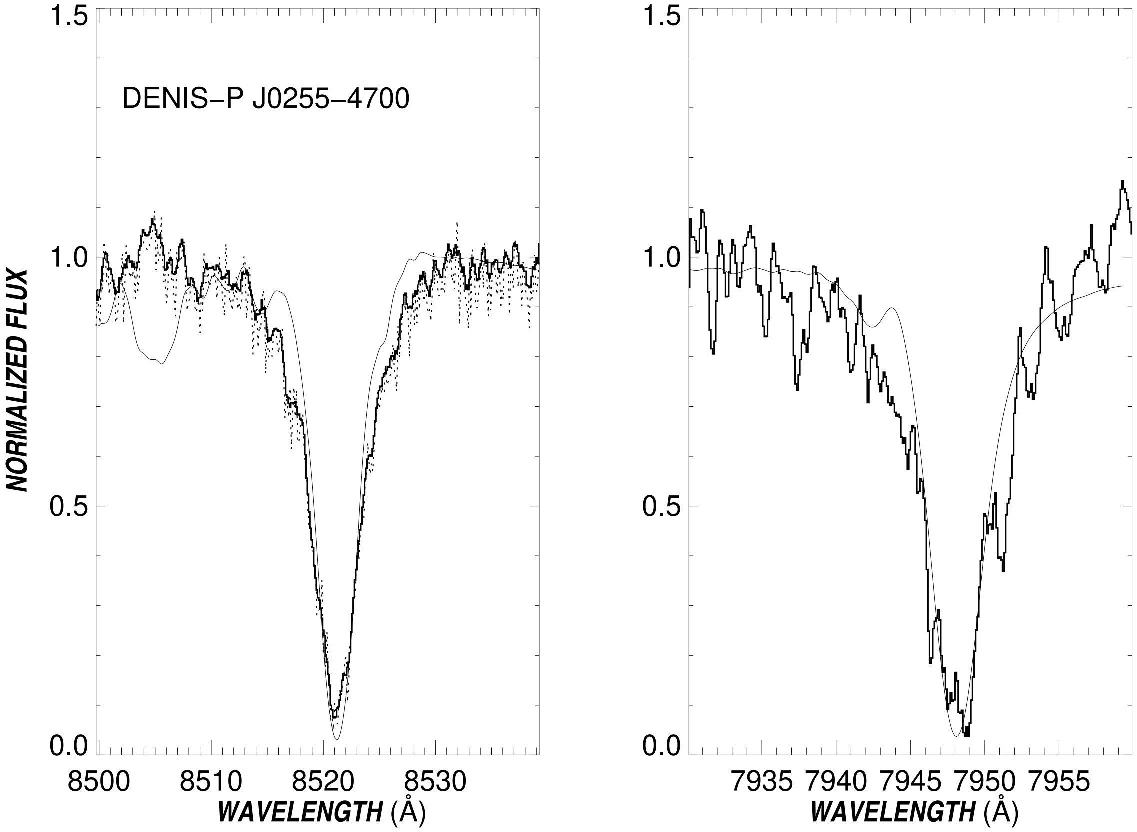

Fig. 19.— *Left panel*: DENIS-P J0255-4700 Cs I spectrum , with 1700K (thin solid line) cleared-dust model at 40 km s^{-1} . Also shown is the unsmoothed data (dotted line) to show the unmodeled molecular lines within the Cs I line, and the unsmoothed depth of the Cs I line. *Right panel*: DENIS-P J0255-4700 Rb I spectrum, with 1900K cleared-dust model at 40 km s^{-1} .

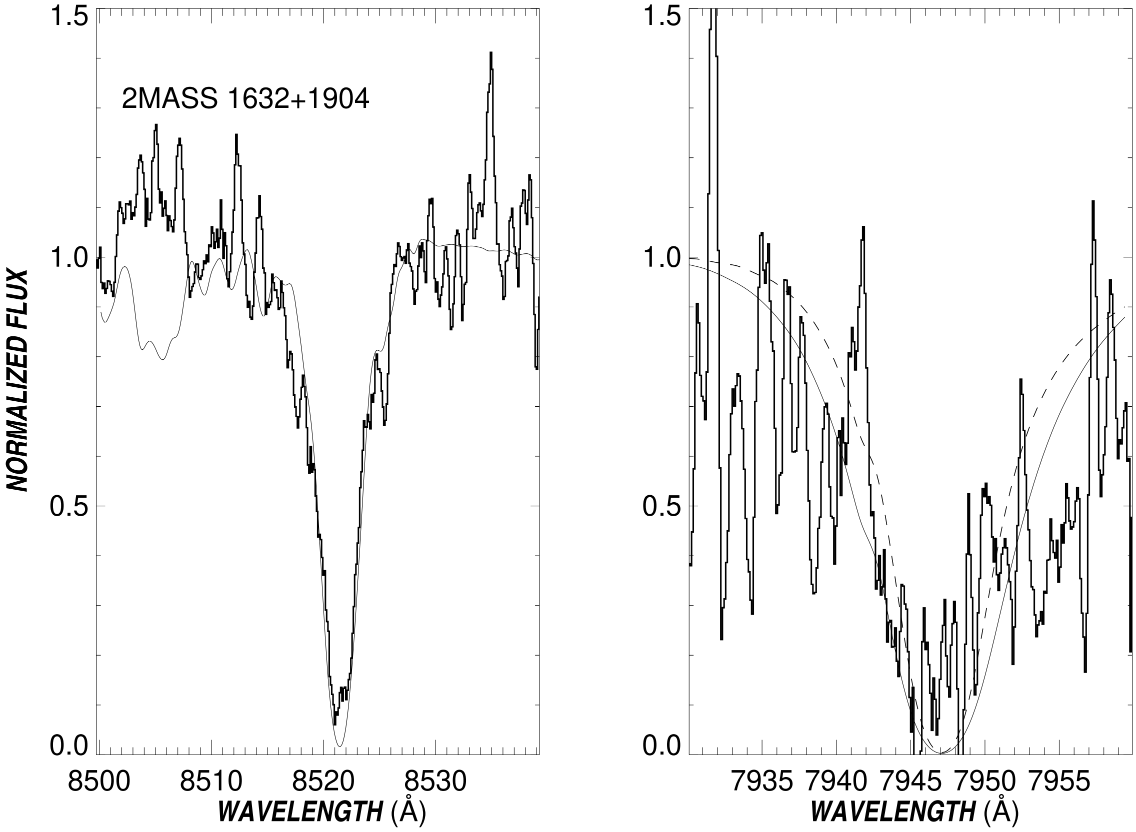

Fig. 20.— *Left panel*: 2MASSW 1632+1904 Cs I spectrum, with 1700K cleared-dust model at 30 km s^{-1} . *Right panel*: 2MASSW 1632+1904 Rb I spectrum, with 1600K (thin solid line) and 1700K (thin dashed line) cleared dust models at 30 km s^{-1} . Due to the low S/N of the Rb I spectrum, no best fit was found; the models are shown as only very tentative fits, and for comparison to the Cs I fit.

Table 1. Observational Sample.

object	obs. date	spectral type	I-K	v_{rad} km s^{-1}
Gl 406 (LHS 36)	7 Dec 1997	M6V	3.31[a]	+19
	2,3 Jun 1997			+43
	11 Dec 1993			+18
	10 Jun 1997			+18
LHS 2924	2,4 Jun 1997	dM9	4.47[b]	-36
LP 944-20	20 Sep 1998	bdM9.5	4.63[b]	+9
DENIS-P J0021-4244	20 Sep 1998	dM9.5	4.58±0.08[c]	+2
DENIS-P J1208+0149	9 Jun 1999	dM9	4.61±0.20[d]	+9
DENIS-P J2146-2153	24,25 May 1998	dL0	–	0
	9 Jun 1999			0
DENIS-P J0909-0658	7 Dec 1997	dL0	4.70±0.12[c]	+25
G196-3B	24,25 May 1998	bdL1	5.79±0.03[e]	0
	10 Jun 1999			0
2MASSW 1439+1929	10 Jun 1999	L1	4.44[f]	-29
Kelu-1	2 Jun 1997	bdL2	5.0[b]	+14
DENIS-P J1058-1548	2 Jun 1997	dL2.5	5.19[b]	+15
2MASSW 1146+2230	10 Jun 1999	L3	4.99[f]	-16
LHS 102B	20 Sep 1998	dL4	5.60±0.10[g]	+30
DENIS-P J1228-1547	2 Jun 1997	bdL4.5	5.43[b]	+1
DENIS-P J0205-1159	7 Dec 1997	dL5	5.28[b]	+7
2MASSW 1632+1904	9,10 Jun 1999	bdL6	6.00[f]	+7
DENIS-P J0255-4700	20 Sep 1998	dL6	5.28±0.10[g]	+20

[a] Basri & Marcy 1995

[b] Leggett et al. 1998

[c] Delfosse et al. 1999

[d] Martín et al. 1999b

[e] Rebolo et al. 1998

[f] Kirkpatrick et al. 1999a; this is I_{spec}-K_s

[g] Delfosse, private communication

Table 2. Derived Characteristics.

Object	$v \sin i$ km s^{-1}	Spec. T.	T$_{eff}$ Cs I K	T$_{eff}$ Rb I K	T$_{eff}$ adopted K	EqW Cs I A	EqW Rb I A
Gl 406	<3	dM6[a]	2800	2700	2800	0.16	0.56-0.67:
LHS 2924	10±1	dM9[a]	2400-2500	2600	2450[b]	0.43	0.75-0.92:
LP 944-20	30±2.5	bdM9[c]	2400	2600	2400	0.6	0.94
DENIS-P J1208+0149	10±2.5	dM9[a]	2200-2300	2500	2250	0.65	1.2:
DENIS-P J0021-4244	17.5±2.5	dM9.5[d]	2300	2400-2500	2300	0.86-0.93:	1.14:
DENIS-P J2146-2153	10±2.5	dL0[d]	2200	2400	2200	1.2	1.42-1.58:
DENIS-P J0909-0658	25±2.5	dL0[a]	2200	2400	2200	0.85	1.5
G196-3B	10±2.5	bdL1[a]	2200	2400	2200:	1.02	1.52-1.84:
2MASSW 1439+1929	10±2.5	L1[c]	2100-2200	2300	2150	1.33	2.05
Kelu-1	60±5	bdL2[a]	2000	2200	2000	1.7	2.54
DENIS-P J1058-1548	37.5±2.5	dL2.5[a]	1900-2000	2000	1950[b]	2.2	3.35
2MASSW 1146+2230	32.5±2.5	L3[c]	1900-2000	2100	1950	2.09	3.3-3.6:
LHS 102B	32.5±2.5	dL4[a]	1800-1900	1900	1850[b]	3.05	5.5
DENIS-P J1228-1547	22±2.5	bdL4.5[a]	1800	1900	1800	3.7	-
DENIS-P J0205-1159	22±2.5	dL5[a]	1700-1800	-	1750[b]	4.2	-
2MASSW 1632+1904	30±2.5	bd:L6[a]	1700	-	1700	5.01	-
DENIS-P J0255-4700	40±2.5	bd:L6[a]	1700	1900	1700[b]	5.75	5.3::

[a]Martín et al. 1999b

[b]Martín et al. 1999b attribute to us a slightly different T$_{eff}$ for this object; they used our preliminary fits, which have been revised.

[c]Kirkpatrick et al. 1999a

[d]assigned in this paper, based on our derived T$_{eff}$ and the spectral-type assigned by Martín et al. 1999b to an objects with similar T$_{eff}$